Azimuthal Anisotropy From Multimode Waveform Modeling Reveals Layering Within the Antarctica Craton

Caroline Beghein [*][1], **Haotian Xu** [1]

[1]Department of Earth, Planetary, and Space Sciences, University of California Los Angeles, Los Angeles, CA, USA

Author contributions: *Conceptualization*: C. Beghein. *Methodology*: C. Beghein, H. Xu. *Software*: H. Xu. *Formal Analysis*: C. Beghein, H. Xu. *Writing - original draft*: C. Beghein. *Visualization*: H. Xu. *Supervision*: C. Beghein.

Abstract   The isotropic structure of the crust and upper mantle under Antarctica has been constrained by many studies. However, the depth dependence of seismic anisotropy, a powerful tool to characterize deformation and flow, is still poorly known. Here, we modeled three-dimensional (3-D) variations in azimuthal anisotropy under Antarctica using a multimode Rayleigh waveform fitting technique. We first searched the model space with a reversible-jump Markov Chain Monte Carlo approach to find path-averaged vertically polarized shear wave velocity profiles that fit fundamental and higher mode Rayleigh waveforms. We then inverted them to obtain a 3-D velocity and azimuthal anisotropy model across the region down to 600 km depth. Our results reveal that the east-west dichotomy found in other studies is not only characterized by different wave velocities but also by different anisotropy directions, likely reflecting the different deformation histories of the two blocks. Azimuthal anisotropy was found to be present in the top 300 km only and peaks at 100 — 200 km depth under the East Antarctica craton. Additionally, depth changes in fast direction were observed within the craton between 75 km and 150 km depth, suggesting layering is present. We speculate this layering relates to the formation history of the craton.

Non-technical summary   The Antarctica plate holds important clues regarding continent formation and evolution. The dependence of the speed of seismic waves with the wave direction of propagation provides unique information about the deformation history of the crust and mantle. However, few studies so far have constrained the depth extent of the anisotropy below 200 km depth. Here we use recordings of distant earthquakes over a 15 year period at seismometers across and around Antarctica to investigate the presence of anisotropy down to 600 km depth. We find that anisotropy is present across the continent in the upper 300 km but not deeper. There is also a striking difference in the fast wave direction between the oldest part of Antarctica to the East and the younger West Antarctica. Our results also indicate a vertical change in anisotropy between

*Corresponding author: cbeghein@ucla.edu

33 75 km and 150 km depth under the oldest, most stable part of the continent. We speculate it relates

34 to compositional changes linked to the building of the history of formation of the continent.

1   Introduction

1.1   Tectonic Setting

37 The Antarctica plate, which includes the Antarctica continent, the Kerguelen Plateau, and oceans, is one of the largest

38 plates on Earth. It is interesting from a tectonics and geodynamics point of view as its structure holds important clues

39 regarding the reconstruction of the supercontinent Gondwana (e.g. Boger, 2011; Ebbing et al., 2021). It also moves

40 relatively slowly compared to other large plates (at 1.89 cm/yr in West Antarctica in a no-net rotation reference (NNR)

41 frame (Accardo et al., 2014)). The continent can be divided into two distinct regions (Fig. 1): East Antarctica (EANT),

42 which is believed to be a Precambrian craton, and West Antarctica (WANT), which is composed of several crustal

43 blocks dating back to the Jurassic (Dalziel, 1992; Anderson, 1999). Between EANT and WANT, the 3,500 km-long

44 Transantarctic Mountains (TAMs) extend from Victoria Land in the South to the Weddell Sea in the North (Fitzgerald,

45 2002). A notable feature at the center of EANT is the high elevation (>2,000 m) Gamburtsev Subglacial Mountain

46 (GSM) chain, but its age and origin are not well constrained because they are hidden beneath the East Antarctic Ice

47 Sheet (Ferraccioli et al., 2011). WANT includes the West Antarctic Rift System (WARS), a striking geological feature

48 that experienced extension starting after the break-up of Australia and Antarctica 95 Ma ago, and that has been active

49 during most of the Cenozoic (e.g. Behrendt, 1999; Wörner, 1999; Granot et al., 2010). A thermal anomaly related to

50 this extension is thought to be present in the WANT asthenosphere (An et al., 2015a). WANT is also comprised of the

51 Marie Byrd Land (MBL), which is associated with recent volcanism that might have resulted from the rifting or that

52 may instead reflect the signature of a mantle plume (Behrendt et al., 1991) as suggested by seismology (e.g. Sieminski

53 et al., 2003; Accardo et al., 2014; Emry et al., 2015) and geochemistry (Wörner, 1999).

1.2   Seismic Velocities

55 Early seismological studies of Antarctica generally suffered from poor resolution due to the paucity of seismic stations

56 (e.g. Press and Gilbert, 1959; Evison et al., 1960; Kovach and Press, 1961; Dewart and Toksöz, 1965; Roult et al., 1994;

57 Sieminski et al., 2003). However, seismic deployments over the past two decades have greatly improved data coverage

58 and have led to several higher resolution models of the Antarctic crust and upper mantle (e.g. Heeszel et al., 2013;

59 Hansen et al., 2014; An et al., 2015b; Lloyd et al., 2015).

60   Seismological studies generally agree that EANT is characterized by a thick crust and a deep root with relatively

61 fast seismic velocities that are typically representative of stable continents, whereas WANT displays lower velocities

62 and a thinner crust (Roult et al., 1994; Danesi and Morelli, 2000, 2001; Ritzwoller et al., 2001; Sieminski et al., 2003;

63 Watson et al., 2006; Hansen et al., 2010; Heeszel et al., 2013; An et al., 2015b; Lloyd et al., 2020) and no clear signature

64 of a fast lid (Ritzwoller et al., 2001). The first estimates of Moho depths (Evison et al., 1960; Kovach and Press, 1961;

65 Dewart and Toksöz, 1965) were around 35 − 40 km and 25 − 30 km for EANT and WANT, respectively. More recent

66 analyses show an average Moho of ∼40 km in the central EANT region, 19 − 29 km for WARS (Ramirez et al., 2016),

and 43 — 58 km underneath the GSM (Hansen et al., 2009, 2010; Ramirez et al., 2016). The latter is generally larger than the 40 km from gravity analyses at the GSM (Block et al., 2009). For the Ross Sea, the WANT crustal thickness ranges between 16 and 25 km (Winberry and Anandakrishnan, 2004; Lawrence et al., 2006; Pyle et al., 2010; Finotello et al., 2011; Chaput et al., 2014; Ramirez et al., 2017). At MBL, values of 20 — 35 km have been reported (Ramirez et al., 2016, 2017). Ramirez et al. (2016) additionally estimated heat flow from their Moho depth measurements and the age of the crust. They found values under the GSM and the Wilkes Subglacial Basin (WILK) similar to Precambrian terrains on other continents where heat flow has been measured.

Most studies point to a maximum lithospheric thickness of around 250 km under EANT, though most do not have great vertical resolution below that depth. In the first tomographic model of Antarctica, Roult et al. (1994) detected a structure characterized by fast seismic velocities down to depths of about 250 km under EANT. Ritzwoller et al. (2001) found similar values with a continental root of 220-250 km and no low-velocity zone, and Danesi and Morelli (2001) reported values of at least 200 km. New surface wave analyses of fundamental mode phase (Heeszel et al., 2013) and group (An et al., 2015b) velocities show similar and consistent results for EANT: the Gamburtsev Subglacial Mountains (GSM) are underlaid by a thick crust ($\sim$60 km) and a seismically fast cratonic lithosphere reaching deeper than 200 km. The exception is the full-waveform adjoint tomography of Lloyd et al. (2020) that led to a greater cratonic thickness between 250 km and 350 km.

The TAMs as well as the ocean ridges surrounding the Antarctic continent are generally characterized by low velocities mostly confined to the upper 150 km (Roult et al., 1994; Danesi and Morelli, 2001; Watson et al., 2006). The volcanism at the Victoria Land segment of the TAMs (e.g. Mount Erebus) is commonly thought to have a deep mantle origin (Emry et al., 2020) and is often attributed to mantle plumes (LeMasurier and Landis, 1996). A localized low-velocity region down to about 200 km depth under the Ross Island volcanic complex was also detected (Danesi and Morelli, 2001; Watson et al., 2006), superimposed to the broader anomaly associated with the WARS (Morelli and Danesi, 2004; Danesi and Morelli, 2001). Based on the inversion of fundamental and higher mode Rayleigh waves dispersion, Sieminski et al. (2003) argued that this relatively slow structure extends into the mantle transition zone (MTZ) and indicates the presence of a mantle plume. A number of recent regional seismic tomographic results have also shown relatively low seismic velocities under the MBL extending through the upper mantle and possibly into the mantle transition zone (Hansen et al., 2014; Lloyd et al., 2015; Heeszel et al., 2016; Lloyd et al., 2020). In contrast, Emry et al. (2015) detected a local thinning of the transition zone, which may indicate high mantle temperatures, beneath neighboring areas of MBL rather than right below MBL.

1.3 Seismic Anisotropy

Seismic anisotropy, i.e., the directional dependence of seismic wave velocity, offers a more complete description of Earth's elastic structure than isotropic velocities alone. It is also a powerful tool to constrain patterns of deformation in the mantle or the crust (e.g. Becker et al., 2003; Karato et al., 2008; Volk et al., 2021). Anisotropy can manifest itself in different ways in seismic observations: (1) Azimuthal anisotropy, which describes the dependence of seismic wave speeds on the propagation azimuth; and (2) transverse isotropy, in which case the elastic medium has one axis of symmetry. The wave speed differs along the symmetry axis and in the orthogonal direction. This type of anisotropy is referred to as radial anisotropy if the symmetry axis points toward the center of the planet (radial direction).

Two different mechanisms can yield observations of seismic anisotropy: The shape-preferred orientation (SPO) of isotropic structures with contrasting elastic properties and the lattice-preferred orientation (LPO) of the crystallographic axes of elastically anisotropic minerals. LPO of olivine is the generally accepted explanation for observations of seismic anisotropy in the upper mantle as its crystals are highly anisotropic (about 18% shear-wave anisotropy) and is thought to be the dominant material at those depths (Karato and Wu, 1993). In addition, most olivine deformation fabrics tend to align the fast axes of individual olivine crystals in the direction of shear. In the case of horizontal mantle flow induced by a vertical velocity gradient, the rule of thumb is thus that the fast direction for seismic waves reflects the flow direction. Consequently, observations of seismic anisotropy with axes aligned with present-day plate motion in regions of low seismic velocities are often interpreted as the signature of current mantle flow in the asthenosphere (e.g. Gung et al., 2003; Marone et al., 2007; Beghein et al., 2014). In the mantle lithosphere, it has been interpreted as the signature of fossil- or paleo-directions of deformation (e.g. Silver, 1996; Smith et al., 2004). Seismic anisotropy has also been detected at greater depths, including in the mantle transition zone (e.g. Fouch and Fischer, 1996; Trampert and van Heijst, 2002; Visser, 2008; Yuan and Beghein, 2013; Auer et al., 2014; Yuan and Beghein, 2014; Huang et al., 2019), top of the lower mantle (e.g. Lynner and Long, 2015; Ferreira et al., 2019), and in the lowermost mantle (e.g. Panning and Romanowicz, 2006; Lynner et al., 2014), but its interpretation at those depths is more uncertain.

Shear-wave splitting (e.g. Silver and Chan, 1988; Long and van der Hilst, 2005) is one of the most common types of seismic observations that can directly detect the presence of seismic anisotropy, and a number of researchers have applied this technique to Antarctica (e.g. Pondrelli and Azzara, 1998; Barruol and Hoffmann, 1999; Müller, 2001; Pondrelli et al., 2006; Bayer et al., 2007; Reading and Heintz, 2008; Barklage et al., 2009). With the seismometers deployed for the POLENET/ANET project, Accardo et al. (2014) carried out analyses of azimuthal anisotropy for WANT. They found that the fast axis directions for shear waves consistently show large angles with the Absolute Plate Motion (APM), which may indicate that the uppermost mantle is subject to a secondary convection mechanism other than plate motion. They also found a radial pattern of fast axis direction inland from the Amundsen Sea around the MBL dome, which was interpreted as flow associated with a mantle plume head.

Another body wave technique, based on P-wave travel times, was also applied to data collected by multiple arrays in northeast Antarctica, covering the northern TAMs, the WILK, and the Terror Rift, which is located at the westernmost edge of the WARS (Zhang et al., 2020). The authors detected lateral variations in P-wave radial anisotropy at depths < 300 km with a fast horizontal direction associated with past tectonic events under the northern TAMs. They also found that the Terror Rift is associated with a fast vertical direction, which they attributed to local asthenospheric upwelling. The same study revealed a high-velocity zone under the TAMs and below 300 km depth, which, combined with the radial anisotropy, was interpreted as being due to a foundering lithosphere or a delaminated slab.

Body wave analyses provide good lateral resolution, but they lack vertical resolution because measurements result from near-vertical paths and thus reflect the integrated effect of the (anisotropic) structures encountered along the path. Surface waves constitute another type of data that can be used to model seismic anisotropy (e.g. Anderson, 1962; Montagner and Nataf, 1986; Ekström and Dziewonski, 1998; Trampert and van Heijst, 2002; Trampert and Woodhouse, 2003). Even though their lateral resolution (of a few hundred of kilometers at best) is lower than that

of body waves, they provide constraints on structure and anisotropy with greater vertical resolution due to their dispersive nature. Roult et al. (1994) obtained the first azimuthally anisotropic phase velocity maps of Antarctica by inverting fundamental mode Rayleigh wave dispersion curves in the period range $60 - 300$ s. Their study, which covered the whole Antarctica continent and its surroundings, showed that oceanic areas are associated with stronger azimuthal anisotropy than continents and that the TAMs have relatively large anisotropy within the Antarctica continent. The fast directions of propagation in the oceans were found to be orthogonal to most of the ridges and to align with the direction of plate motion. However, the ray path coverage was very limited due to the small number of stations available, with only $\sim$400 paths covering the southern hemisphere. Ritzwoller et al. (2001) performed another continental-scale study of the region and reported an average of $\sim$4 % radial anisotropy for Antarctica and surrounding areas, with slightly stronger amplitudes in WANT than in EANT.

Additionally, with data from the Transantarctic Mountain Seismic Experiment, Lawrence et al. (2006) measured Rayleigh wave dispersion under the Ross Sea, the TAMs, and EANT with an interstation technique, and detected 1.5 — 3% azimuthal anisotropy beneath EANT with a NE-SW fast direction at periods between 20 and 120 s, corresponding to depths of $\sim$30 $-$ 160 km. They attributed this anisotropy to LPO within a cold continental lithosphere due to past deformation such as the Ross Orogeny. It should be noted that because their anisotropy model was found to be reliable only at the intersection of the two seismic arrays they used, they did not have constraints on the lateral extent of the anisotropy.

More recently, seismic anisotropy was also discovered in the crust and uppermost mantle across WANT and central Antarctica using ambient noise tomography in the period range 8 — 25 s (O'Donnell et al., 2019; Zhou et al., 2022, 2023). Radial anisotropy with horizontally polarized shear (SH) waves faster than vertically polarized shear (SV) waves and azimuthal anisotropy were found in the shallow crust. The fast direction of the azimuthal anisotropy is subparallel to the inferred extension direction of the West Antarctic Rift System (Zhou et al., 2023). This is consistent with LPO of minerals such as mica and amphibole in extensional settings. Most of West and Central Antarctica display a mid-to-lower crust with $V_{SV} > V_{SH}$ instead, potentially due to LPO of plagioclase under extension. The uppermost mantle under WANT was shown to be characterized by $V_{SH} > V_{SV}$, interpreted as olivine LPO due to tectonic activity (Zhou et al., 2022). This is supported by the azimuthal anisotropy fast direction that generally aligns with shear wave splitting fast axes and suggests a thin lithosphere (Zhou et al., 2023).

Because body wave studies have limited vertical resolution and the surface wave results discussed above were based on data that cannot resolve structure below ~ 200 km, the depth extent of seismic anisotropy under Antarctica is still poorly known. Higher mode surface waves have the potential to improve our constraints on the depth dependence of anisotropy as they are sensitive to much larger depths than fundamental mode surface waves or ambient noise data. To the best of our knowledge, only two studies of Antarctica have utilized such surface wave overtones: (1) Sieminski et al. (2003), who found the presence of azimuthal anisotropy to be significant in the upper 200 km underneath the Antarctica continent, with maximum amplitudes at 100 km depth, and decreasing to less than 1 % below 200 km, and (2) Lloyd et al. (2020), but they did not interpret the radial anisotropy structure retrieved due to an imbalance in sensitivity of the speed of SV and SH waves.

In this paper, we took advantage of the increased number of available seismic stations in Antarctica since the study

of Sieminski et al. (2003), and we obtained a new three-dimensional azimuthally anisotropic model for SV waves down to 600 km depth by jointly inverting fundamental and higher mode Rayleigh waveforms. We first present the data and methods employed, present our model, and interpret it in terms of deformation mechanisms. We then put it in the context of previous surface wave and shear wave splitting studies.

2 Data Selection

The seismic data coverage in Antarctica was boosted significantly by the deployment of temporary seismic networks (e.g., TAMSEIS (Anandakrishnan and Wiens, 2000), GAMSEIS (Wiens and Nyblade, 2007a), POLENET (Wiens and Nyblade, 2007b), TAMNNET (Hansen, 2012), UKANET (Brisbourne, A. et al., 2016)). In this study, we considered permanent and temporary seismic stations south of -40 degrees latitude and collected data recorded between 2005 and 2020. Because the lateral resolution of the models is limited by the wavelength of the surface wave data utilized, performing measurements at nearby stations would not improve resolution. The minimum interstation distance was thus set at 75 km so that only a few stations from dense arrays are used. The list of stations and networks employed can be found in Tab. S1. The selected 168 stations are shown in Fig. 2.

We considered all events recorded at these stations between 2005 and 2020 and falling between -20 degrees to -90 degrees latitude. We obtained the event source parameters from the GCMT catalog (Dziewonski et al., 1981; Ekström et al., 2012), and selected events with moment magnitudes Mw between 5.5 and 7.0. The magnitude thresholds were chosen to avoid small magnitude earthquakes with a low signal-to-noise ratio (SNR), and to avoid large magnitude earthquakes that cannot be approximated by the single point source assumption in waveform modeling. The station-event pairs were then selected based on the following criteria: 1) The epicentral distance should be between 30 degrees and 75 degrees. The lower bound guarantees that the higher mode waveforms separate adequately from the fundamental mode. We also avoided paths with long epicentral distances as they are more likely to be contaminated by scattering effects (Lebedev et al., 2005); 2) The SNR of the recorded waveform should be higher than 10 for the 10-20 mHz frequency band, and higher than 5 for the 5-10 mHz frequency band. This second criterion helped filter out records contaminated by noise. The lower frequency band had a lower threshold because it usually carries weaker energy compared to the higher frequency band; 3) At least 45 % of the great circle paths had to fall within the Arctic Circle in order to ensure good constraints on the Antarctica Continent. The selected 578 events are shown in Fig. 2 and the corresponding ray coverage is in Fig. 3.

3 Methods

Higher mode surface waves have the advantage of being sensitive to a greater depth range than the traditionally used fundamental mode surface waves at the same periods. They are also dispersive and this dispersion relation can be employed to constrain the depth dependence of seismic wave velocities and anisotropy. Measuring higher modes surface wave dispersion is, however, challenging because their group velocities overlap significantly in a broad frequency range. Therefore, direct measurement methods that work for fundamental mode surface waves cannot be applied to higher modes due to the difficulties in separating different modes. Waveform fitting techniques have been favored by multiple researchers instead (Stutzmann and Montagner, 1993; Montagner et al., 1994; Beucler et al., 2003;

Yoshizawa and Kennett, 2002, 2004; Yoshizawa and Ekström, 2010; Visser et al., 2007; Visser, 2008; Xu and Beghein, 2019). In this study, we opted to use the waveform-fitting method developed by Xu and Beghein (2019). It was initially designed to separate different modes and measure single-station phase velocity dispersion curves for fundamental mode surface waves and overtones, which in turn can be inverted for structure. Our waveform modeling approach can also be used directly to obtain a 3-D interior model, which is what we opted to do in this study, as explained below.

3.1 Waveform Fitting

The method employed makes use of a reversible-jump Markov Chain Monte Carlo (rj-MCMC) approach (Bodin and Sambridge, 2009; Bodin et al., 2012) and performs a transdimensional model space search to seek a large number of path-averaged one-dimensional (1-D) shear wave velocity (V_S) models that fit the filtered waveform. Here, we filtered the waveforms between 50 s and 200 s period. In the original version of the software, the resulting 1-D models, which represent the average fundamental and higher-mode dispersion curves for the chosen source-receiver path, were employed to calculate dispersion curves. A reliability analysis was performed afterwards to determine which overtones had been reliably separated. Here, we invert the 1-D path-averaged models instead to construct a 3-D model of shear-wave velocities and anisotropy and skip the phase velocity dispersion estimate (see details in section 3.2).

A synthetic seismogram, denoted by s, can be calculated by summation of normal modes, m, in the frequency domain for a 1-D model as follows (Dahlen, 1968):

$$s(\omega) = \sum_m A_m(\omega) exp[i\omega\Delta/c_m(\omega)] \tag{1}$$

where $c_m(\omega)$ is the phase velocity of mode m at angular frequency ω, A_m is its amplitude, and Δ is the epicentral distance. The relationship between seismograms and their corresponding velocity model is thus highly non-linear. The computation of normal mode eigenfunctions and eigenfrequencies for a given mantle model is time-consuming and thus we cannot use the fully non-linear formulation of Eq. 1 at each of the hundreds of thousands of iterations of the MCMC scheme. The forward modeling problem was thus linearized to overcome computational speed limitations as detailed in the next paragraph.

A synthetic seismogram is first obtained for a chosen reference model using the fully non-linear formulation of Eq. 1 and FORTRAN package Mineos (Masters et al., 2011). Perturbation theory is then applied to update the seismogram for the models generated at each iteration of the Markov Chain. For a small perturbation, the change in mode eigenfrequency can be calculated assuming unperturbed eigenfunctions:

$$\delta\ln(\omega) = \int_0^a (\frac{\delta V_P}{V_P}(r)K_{V_P}(r,\omega) + \frac{\delta V_S}{V_S}(r)K_{V_S}(r,\omega) + \frac{\delta\rho}{\rho}(r)K'_\rho(r,\omega))dr + \sum_d \delta d[K_d(\omega)]^+_- \tag{2}$$

where $\delta\ln(\omega) = \delta\omega/\omega$, a is the radius of the Earth, and V_P, V_S, ρ and d are P-wave velocity, S-wave velocity, density, and radius of discontinuities, respectively. $K_{V_P}, K_{V_S}, K'_\rho$ and K_d are the Fréchet derivatives, which relate the change in wave velocities, density, and depth of discontinuity from the reference model to changes in the eigenfrequencies. The Fréchet derivatives are calculated for each mode using the eigenfunctions determined for the reference model (Woodhouse, 1980). The updated eigenfrequency ω^* can be converted into phase velocity for a normal mode of

angular order l using (Jeans, 1923):

$$c(\omega^*) = \frac{\omega^* a}{l + 0.5} \tag{3}$$

The isotropic nature of the model is assumed at this stage of the modeling for computational reasons. Visser (2008) demonstrated that it is a reasonable assumption for individual oaths, and seismic anisotropy can be estimated at a later stage. As in Xu and Beghein (2019), the V_S profile is parameterized with a variable number of interpolation points. The vertical position of these points is the depth at which V_S is perturbed and their horizontal position is the amount by which V_S is perturbed relative to the reference model within a velocity prior. Here the prior for V_S is 10 per cent of the velocity in the reference model at a given depth. While in theory, all parameters (V_S, V_P, ρ, and d) could be perturbed independently, surface waves typically can only resolved V_S due to the existence of strong trade-offs between model parameters. Because of this and to reduce computational costs, we scaled δV_P and $\delta \rho$ to δV_S using $\delta \ln V_P = m_\alpha \delta \ln V_S$ and $\delta \ln \rho = m_\rho \delta \ln V_S$. For the P-wave scaling, we used a linearly varying scaling relation with $m_\alpha = 0.8$ at the surface and $m_\alpha = 0.565$ at 800 km depth (Montagner and Nataf, 1986). For the density scaling, we used $m_\rho = 0.3$ (Anderson et al., 1968). Many studies have demonstrated that these choices do not affect the V_S models (e.g., Panning and Romanowicz, 2006; Beghein, 2010), and Visser (2008) showed that P-wave velocity and density have little influence on the phase velocity perturbation in the frequency range considered (5—20 mHz). Meier et al. (2009) also showed that higher modes cannot resolve perturbations in the depth of deep mantle discontinuities. We thus opted to neglect perturbations in d except for the Moho which was allowed to vary by ± 2 km at each iteration.

In order for the MCMC sampling algorithm to converge within a reasonable amount of time, to reduce the errors introduced by the linearization of the forward modeling, and to avoid cycle skipping, our waveform inversion technique requires a good 1-D reference model. In addition, it has been shown that the Moho depth can have non-linear effects on waveform modeling and phase velocity calculations (Montagner and Jobert, 1988). It is thus preferable for the reference model to have a crust that is representative of the (path-averaged) regional crust rather than using a 1-D globe average such as the Preliminary Reference Earth Model (PREM, Dziewonski and Anderson (1981)) for instance. For each event-station pair, we thus calculated a path-averaged reference model using CRUST1.0 (Laske et al., 2013) and 3-D global model 3D2018_08Sv (Debayle et al., 2016), and computed the corresponding shear-wave sensitivity kernels. While there exist more recent, region-specific crustal models (e.g. Chaput et al. (2014); An et al. (2015b)), their Moho depths only differ significantly from CRUST1.0 (around 40 km) in relatively small, localized areas compared to the length of our ray paths and the long wavelengths of our data: An et al. (2015b) report $55 - 60$ km at the GSM, ~ 50 km along the EANT Mountain Ranges, and around 30 km in northern WANT and $20 - 25$ km in southern WANT. In addition, many of our paths sample even greater changes in crustal thickness since they traverse the thin oceanic crust (with a Moho depth close to 5 km), which is well approximated by CRUST1.0, in addition to the thicker continental crust. This, in addition to the fact that the algorithm iteratively modifies the crust and mantle models, means that the path-average model calculated using CRUST1.0 and 3D2018 is a good representation of the average structure and serves our purpose.

The rj-MCMC scheme employed here performs a guided Monte Carlo sampling of the model space using the misfit between the real and the synthetic seismograms. As explained in Xu and Beghein (2019), the method fits seismic waveforms in multiple frequency-time windows, which are chosen using group velocities and S- or SS-wave arrival

times such that they include the fundamental and several higher modes. The criteria used to select those windows are summarized in Tab. 1. The synthetic waveforms and the recorded waveforms were compared in those windows and the total misfit function is given by:

$$\text{Misfit}(\mathbf{m}) = \sum_{j=0}^{M} \frac{\sum_{i=0}^{N_j}(d_{j,i} - s_{j,i})^2}{\sum_{i=0}^{N_j} d_{j,i}^2} \tag{4}$$

where $\mathbf{m}$ is the model vector, and $\mathbf{d}$ and $\mathbf{s}$ denote the recorded waveform and synthetic waveform, respectively. M is the number of frequency-time windows while N is the respective number of data points within each window. The normalization factor in the denominator guarantees that the misfits are independent of the absolute amplitudes of earthquakes and are used here for easier quality control. In this study, we sampled a total of 480,000 models and used an ensemble of 1,600 models after the burn-in period for each event-station pair. Examples of waveform fit are shown in Fig. 4.

3.2 Inversions

At each depth z, the path-averaged wave slowness along great circle path l can be expressed as the integral of the local slowness along the great circle path:

$$\frac{1}{V_l(z)} = \frac{1}{d_l} \int_l \frac{1}{V(z,l)} dl, \tag{5}$$

where d_l denotes the epicentral distance for path l and $V_l(z)$ is the wave speed along the path. We applied our MCMC method to each of the 2,000 paths that passed the above-described quality control, resulting in 1,600 velocity profiles $V_l(z)$ for each event-station pair after the burn-in period. We used the mean and standard deviation of these 1,600 velocity profiles to build a 3-D azimuthally anisotropic velocity model as described below.

In a slightly anisotropic medium, the azimuthal variation of SV-wave propagating horizontally with velocity V_{SV} can be expressed as (Montagner and Nataf, 1986):

$$V_{SV}(z,\Psi) = V_0(z) + A_1(z)cos(2\Psi) + A_2(z)sin(2\Psi) + B_1(z)cos(4\Psi) + B_2(z)sin(4\Psi) \tag{6}$$

where Ψ denotes the propagation azimuth. We inverted our ensemble of path-averaged velocities $V_{SV}(z,\Psi)$ at selected depths using a LSQR procedure (Paige and Saunders, 1982) to obtain the isotropic shear-wave velocity $V_0(z)$ and the anisotropic terms $A_1(z)$, $A_2(z)$, $B_1(z)$, and $B_2(z)$. We parameterized the study area with a 2-D triangular grid at each depth, and each $V_{SV}(z,\Psi)$ was weighted using their standard deviation at depth z. In general, the velocity uncertainties increase with depth due to the lower sensitivity of our data set to deeper structure. For instance, most paths have uncertainties smaller than 40 m/s at 60 km and 150 km, but at 600 km the majority of the uncertainties fall in bins larger than 50 m/s (Fig. 5). Shen et al. (2018) reported a standard deviation of $50-65$ m/s from their Bayesian inversion on fundamental surface waves and receiver functions, which are roughly consistent with our path-specific uncertainties above 250 km.

Regularization is needed in order to solve this ill-posed geophysical problem and to avoid over-fitting the data.

We chose to minimize the following cost function:

$$C = \lambda_1 ||\mathbf{Lm}|| + \lambda_2 ||\mathbf{m}|| \tag{7}$$

where $\mathbf{L}$ is a smoothing operator that acts upon the model vector, $||\mathbf{m}||$ is a L_2-norm term that affects the strength of the velocity anomalies, and λ_1 and λ_2 are tuning parameters. Separate tuning parameters were introduced for the isotropic terms, the 2Ψ terms, and the 4Ψ terms. For each parameter, we used the L-curve method (Hansen, 1998) to select the amount of damping. The preferred damping is chosen at the "elbow" of the L-curve, which represents a good trade-off between variance reduction and model complexity. Different depths were treated independently, and at each depth we started by selecting the damping for the isotropic term. After the optimal regularization is selected for the isotropic term, we proceeded with the L-curve for the 2Ψ terms, and finally with the 4Ψ terms. Fig. 6 shows an example of damping selection at 150 km depth. The significance of the 2Ψ and 4Ψ terms is determined using F-tests (Bevington and Robinson, 2002) and is discussed in the Results section.

4   Results

4.1   Significance of the Anisotropy

As shown in Fig. 6, the variance reduction increases as more parameters are included in the inversion. However, this misfit improvement may be due to the increase in the number of unknowns and may not necessarily be required by the data. In order to test if the anisotropic terms are statistically significant, we performed F-tests (Bevington and Robinson, 2002) following Trampert and Woodhouse (2003).

For this purpose, we defined a reduced χ^2:

$$\chi^2 = \frac{1}{N-M}(\mathbf{d} - \mathbf{Gm})\mathbf{C_d}^{-1}(\mathbf{d} - \mathbf{Gm}) \tag{8}$$

where $\mathbf{d}$ is the data vector and $\mathbf{G}$ is a matrix describing the relationships between the data and the model parameters. $\mathbf{C_d}$ is the data covariance matrix, which in our case is a diagonal matrix containing the standard deviations of the models shown in Fig. 5. N is the number of data points and M is the trace of the resolution matrix $\mathbf{R}$, i.e. the number of independent parameters for the chosen regularization. The resolution matrix, and thus M, cannot be directly calculated with the LSQR method. Instead, we calculated it by inverting each column of matrix $\mathbf{G}$:

$$\mathbf{R_j} = \mathbf{LG_j} \tag{9}$$

where $\mathbf{L}$ represents the LSQR operator and $\mathbf{R}_j$ is the j-th column of the resolution matrix. Fig. 7 shows an example of reduced χ^2 at 150 km depth as a function of the trace of the resolution matrix. It demonstrates that the reduced χ^2 decreases as the number of independent parameters increases.

To determine whether the reduction in misfit is significant at each depth, we then performed F-tests and compared the preferred models selected by the L-curve method. In such comparisons, the null hypothesis is that the simpler model and the more complicated model can explain the data equivalently well. The F-test calculates the

10

confidence level at which the null hypothesis can be rejected (i.e., the model with more parameters significantly improves the data fit). Here, we set the confidence level threshold at 85% and found that the misfit reduction between the isotropic inversions and isotropic + 2Ψ inversions are only significant at a depth shallower than 300 km, whereas the misfit reduction between the 2Ψ inversions and the 4Ψ inversions is not significant except at a depth of 60 km. Details of the F-test analysis can be found in Tab. 2. Based on these results, we argue that the presence of the 2Ψ azimuthal anisotropic terms is required by the data in the upper mantle above 300 km, but that the 4Ψ terms are generally not needed. This is consistent with the fact that Rayleigh waves are mostly sensitive to the elastic parameters governing the speed of vertically polarized shear waves, which can be inverted from the 2Ψ coefficients $A_1(z)$ and $A_2(z)$ (Montagner and Nataf, 1986). The 4Ψ coefficients $B_1(z)$ and $B_2(z)$ can be seen as depth integrals of the elastic parameters governing the speed of horizontally polarized shear waves instead (e.g. Yuan and Beghein (2014)). We thus focus our discussion on the isotropic model and the 2Ψ anisotropy.

4.2   Isotropic Model

The isotropic part of our 3-D model is displayed in Fig. 8. Because we used data at periods of 50 s and larger, we do not expect the top 50 km to be well constrained, and thus only present the velocity model below that depth. The dichotomy between EANT and WANT dominates the velocity variations at depths of 60 km, 100 km, and 200 km, which indicates distinct seismic patterns underneath the cratonic EANT and the extensional WARS. The largest amplitude anomalies range from +7% relative to PREM (Dziewonski and Anderson, 1981) underneath EANT to about -5% below WANT. Such strong anomalies start to diminish below 200 km, and at MTZ depths the anomalies are generally within +/- 2%.

Vertical slices of three transects are shown in Fig. 9. Transect A — A' samples both WANT and EANT and shows the clear dichotomy between the two regions with relatively slow shear waves under WANT and relatively fast shear waves under EANT. The negative velocity anomalies under WANT are located between about 80 km and 200 km depth and have a relative amplitude of around 4%. The fast velocity anomalies under EANT extend down to 225 km under the GSM with relative amplitudes as high as 7%, but only extend down to about 150 km toward Dronning Maud Land (DML) in the northeastern part of the grid. Profile B — B' crosses EANT from grid North to grid South and shows similar results: the GSM is characterized by the deepest positive anomalies and the fastest wave speeds whereas the anomalies near the coast are of shallower origin. Profile C — C' samples WANT and features negative velocity anomalies. They extend down to 200 km depth beneath MBL and along the Amundsen Sea coast to the Antarctica Peninsula.

4.3   Azimuthal Anisotropy

Fig. 10 represents the 2Ψ anisotropy at depths of 75 km, 150 km, 225 km, and 285 km, superimposed to the APM based on model NUVEL-1A in the no-net rotation reference frame (Gripp and Gordon, 2002). Stronger azimuthal anisotropy can be observed in the Antarctica interior as well as in WILK at 150 km depth. The amplitude of the anisotropy starts to decrease below 225 km. At 285 km, central Antarctica still has around 1% anisotropy, but everywhere else the amplitude is smaller. This is consistent with our F-tests that showed that the 2Ψ terms are not significant below ~300 km.

11

Abrupt changes in fast directions can also be identified in all four depth slices between WANT and EANT: while the fast seismic axis is roughly subparallel to the APM just east of the TAMs down to 225 km, it is approximately NE-SW west of the TAMs at 75 km and it shows strong lateral variations at 150 km and 225 km depth.

Depth changes are also observed. Note that because the anisotropy amplitude at 285 km is very small, we do not discuss its direction at that depth as it may not be resolved. In WANT, where the APM is oriented grid NW-SE, the fast direction on land near the Amundsen Sea changes from grid NE-SW at 75 km to NW-SE at 150 km depth and changes back to NE-SW at greater depths. While this could be due to vertical trade-offs among model parameters, we consider it unlikely because the sensitivity of the data does not strongly vary laterally at those depths. In EANT, the fast directions of anisotropy show a grid NW-SE dominant direction in the south, roughly following the APM direction at 75 km depth. The fast direction in central and northern EANT rotates from grid NE-SW at 75 km to grid NNW-SSE at larger depths, which also roughly coincides with the APM direction. At 225 km, the fast direction in northern EANT changes again but less so in the southern part of EANT. It should be noted that the edges of EANT, especially the NE grid corner, do not have good azimuthal ray coverage due to the lack of stations. The azimuthal anisotropy in these areas may thus be less reliable compared to regions such as WANT and the center of EANT, which have better azimuthal coverage.

4.4 Synthetic Tests

We implemented synthetic tests to assess the quality of the data coverage and the trade-offs between isotropic and anisotropic model parameters. Fig. 11 shows the tests performed at a depth of 150 km, including an isotropic checkerboard test, an anisotropic (2Ψ) inversion of an isotropic true model, and an anisotropic inversion of an anisotropic true model. Fig. 12 shows an isotropic checkerboard test at 250 km depth.

In the checkerboard test of Fig. 11, the positive and negative anomalies within -70 degrees can be resolved, though some smoothing effects are seen. The resolution in the surrounding oceans is worse than in the continent due to differences in ray path coverage.

In the second test (Fig. 11), small ($< 0.2\%$) anisotropy is visible in the output model, resulting from trade-offs between isotropic and anisotropic parameters. At the transition area between the positive anomalies in EANT and the negative anomalies in WANT, the output anisotropy amplitude reaches 0.6%. Because this amount of anisotropy is much smaller than the anisotropy retrieved from the real data inversion, we argue that the majority of the azimuthal anisotropy in our model comes from the data rather than from trade-off effects.

The recovered amplitude and fast directions in the third test are consistent with the input model over most of the Antarctica continent. Inconsistencies are nevertheless visible in some of the surrounding oceans where the azimuthal coverage is not sufficient. We also note that the isotropic terms in the second and third tests are recovered well, and the amplitudes of the isotropic terms are not significantly affected by the introduction of the anisotropy.

Fig. 12 shows that at 250 km, the input model recovery is less good than at shallower depths. The center anomaly is visible in the output model but with much lower amplitudes. The anomalies around it are smeared out.

5 Discussion

5.1 Isotropic Structure and Lithosphere-Asthenosphere Boundary

Lloyd et al. (2020) identified a negative anomaly extending into the MTZ under MBL, which they associated with a potential mantle plume. We also observe negative velocity anomalies underneath MBL. However, while they are visible in the upper 200 km and between 300 km and 400 km depth, they are almost non-existent between 200 km and 300 km, questioning whether they are part of the same vertical structure. In addition, the lateral spread of these anomalies is large (close to 1500 km), likely because the long wavelength of the surface waves (especially of the higher modes) limits the horizontal resolution of the 3-D model at those depths. It is therefore difficult to confidently conclude that we see the signature of a plume based on our model. In general, our isotropic velocity anomalies are the strongest above 200 km depth, below which they start to decrease down to +/- 2% at MTZ depths. Just like for the plume hypothesis, we refrain from interpreting these MTZ anomalies because of the limited resolution at these depths. Indeed, as shown in Fig. 5, the uncertainties of the path-specific measurements increase with depth while the amplitude of the velocity anomalies decreases. The deeper anomalies are thus less well resolved than the shallower ones.

The isotropic part of our velocity maps shows strong positive anomalies (up to 7%) in EANT extending down to about 225 km under the GSM. On the contrary, they only extend down to about 150 km near DML in the northeastern part of the grid. These results are consistent with Heeszel et al. (2013) and Lloyd et al. (2020) in that both the thickest part of the craton and the fastest wave speed are located under the GSM and the thinnest parts can be found near the coast.

Different proxies can be used to approximate the lithosphere-asthenosphere boundary (LAB) depth. If we use the depth extent of the relatively fast velocity anomalies, our results suggest a thinner lithosphere closer to the coast than in central EANT. It also results in LAB depths consistent with those of Ritzwoller et al. (2001) and Danesi and Morelli (2001) but shallower than in Lloyd et al. (2020) or Heeszel et al. (2013). However, the choice of the velocity contour to determine the depth extent of the positive V_{SV} anomalies is subjective and depends on the amount of regularization applied. Following Bartzsch et al. (2011), we instead approximated the LAB depth as the middle of the interval over which V_{SV} decreases in our isotropic model. Fig. 13 shows the resulting LAB depth for the Antarctic Plate. It demonstrates a clear difference between WANT and EANT with a LAB depth of around 80 km for WANT and around 180 km for central EANT. The estimated values for WANT are in agreement with the 70 — 100 km range obtained by Heeszel et al. (2016). Compared to An et al. (2015a), who defined the LAB as the shallowest position with a temperature crossing the 1330° adiabat, we find a shallower LAB in the center of EANT (around 190 km compared to their 225 km). The difference is likely caused by the different definitions of the LAB and the lower horizontal resolution of our isotropic model due to the use of surface waves and higher modes at longer periods.

5.2 Anisotropy and Cratonic Layering

Global-scale azimuthal anisotropy models resulting from surface wave inversions usually display a good correlation between the fast seismic direction and APM models in regions with a simple tectonic history, such as the astheno-sphere under oceanic plates (Beghein et al., 2014). In regions with a complicated tectonic history, such as conti-

nents, this correlation can be low (Debayle and Ricard, 2013). In addition, the Antarctic continent moves slowly with respect to whole mantle plate motion models (Gripp and Gordon, 2002) and SKS splitting measurements are generally inconsistent with the APM in both the hotspot and the no-net rotation (NNR) reference frames (Accardo et al., 2014). The observed anisotropic fabric is therefore unlikely to result from shear associated with the viscous drag of the Antarctic lithosphere over the asthenosphere. However, the lack of vertical resolution of SKS measurements can cast some doubts on such inferences. Our 3-D anisotropy model is better suited to examine the relation between seismic anisotropy and APM. In Fig. 10, we plotted the APM based on model NUVEL-1A (DeMets et al., 1994) in the NNR reference frame superimposed to the fast seismic wave directions from our model. We first discuss WANT and then EANT.

Over most of WANT, the APM direction is at an angle with the fast seismic directions of our model. Around MBL and the Ellsworth–Whitmore Mountains, the fast directions are dominantly Grid SW — NE at depths shallower than 100 km. At 150 km, east of MBL, the seismic fast directions rotate and align better with the APM in the MBL area. This may imply, contrary to conclusions based on SKS splitting, that the fast direction between $100 - 150$ km indicates olivine LPO due to present-day mantle deformation within the asthenosphere, whereas the azimuthal anisotropy at shallower depth mainly reflects extensive Cenozoic extension including the final pulse of western WARS rifting in the Miocene (Accardo et al., 2014). At greater depths, the fast direction in WANT changes again and does not reflect the APM direction. We refrain, however, to interpret the depth changes in anisotropy in this part of Antarctica because WANT is relatively small compared to EANT and WANT anisotropy may suffer from smoothing and from the lateral resolution of our data.

For EANT, the fast directions do not match the APM at 75 km and may reflect frozen-in anisotropy within the shallow lithosphere. On the contrary, at 150 km depth and 225 km depth, the fast seismic directions are roughly subparallel to the APM. This is, however, likely too shallow to reflect asthenospheric present-day deformation since the estimated LAB depth for the East Antarctica Craton is around 200 km under the GSM (Fig. 13) and possibly deeper (Lloyd et al., 2020). We propose that this change in fast directions between 75 km and 150 km depth indicates the presence of a second layer in the thick cratonic lithosphere. Similar changes with depth of the fast axis direction of azimuthal anisotropy have been observed within other cratons (e.g., North American craton (Snyder and Bruneton, 2007; Yuan and Romanowicz, 2010; Yuan et al., 2011) and sometimes coincide with the depth of seismic discontinuities (e.g., Foster et al., 2014; Bodin et al., 2016). Depth variations in anisotropic properties have also been reported by authors using anisotropic receiver function analyses in Australia (Wirth and Long, 2014; Chen et al., 2021; Birkey and Ford, 2023). These changes coincide with seismic discontinuities and reveal the presence of layers within the cratonic lithosphere (e.g., Foster et al., 2014; Bodin et al., 2016). This layering likely reflects tectonic events related to the assembly and evolution of the craton.

5.3 Comparison with SKS Splitting

The observation of shear-wave splitting is a direct indication of seismic anisotropy along the path taken by the phase considered (see review by Savage (1999)). It can thus be useful, though not straightforward, to predict shear-wave splitting delay times and fast directions from our 3-D model and compare them with measurements. Montagner et al. (2000) showed that a 3-D azimuthally anisotropic model can be used to predict SKS delay times δt and their fast

488 directions Ψ under the assumption of weak anisotropy with a horizontal axis of symmetry:

$$\delta t = \sqrt{\left(\int_0^R \frac{G_s}{V_{SV}L}dr\right)^2 + \left(\int_0^R \frac{G_c}{V_{SV}L}dr\right)^2} \tag{10}$$

490 and

$$\tan 2\Psi = \frac{\int_0^R \frac{G_s}{V_{SV}L}dr}{\int_0^R \frac{G_c}{V_{SV}L}dr} \tag{11}$$

492 where R is the planet's radius, and $L = V_{SV}^2/\rho$ is the Love elastic parameter of the isotropic model. G_c and G_s

493 are the 2Ψ elastic parameters that govern the azimuthal anisotropy amplitude $G = \sqrt{G_s^2 + G_c^2}$ and fast direction

494 $\Theta = \frac{1}{2}\arctan(G_s/G_c)$ of SV waves. Although comparing predictions from a long-wavelength surface wave model

495 with measurements from body waves is not straightforward due to their different vertical and horizontal resolutions,

496 it can sometimes inform us about the depth of origin of the measured shear-wave splitting.

497 We calculated the predicted SKS splitting delay times and fast directions using the above two equations and our

498 azimuthally anisotropic model between depths of 60 km and 300 km, where the anisotropy was shown to be required

499 by our data. The predictions shown in Fig. 14 are compared with previous SKS splitting measurements in Antarctica

500 (Müller, 2001; Pondrelli et al., 2006; Bayer et al., 2007; Reading and Heintz, 2008; Barklage et al., 2009; Hernandez

501 et al., 2009; Salimbeni et al., 2010; Accardo et al., 2014; Graw and Hansen, 2017; Lucas et al., 2022). We note that

502 we only plotted available SKS measurements with good quality from these previous studies and that some of SKS

503 measurements present large uncertainties in both SKS delay time amplitudes and fast directions. The thick black

504 bar located at the GSM represents the overall splitting directions from Hernandez et al. (2009).

505 Overall, our predicted splitting times roughly agree with the observations in WANT with a dominant fast splitting

506 direction grid SW — NE at EWM, WARS, and MBL. Since the wave fast direction of our model changes from grid SW

507 — NE in the top 150 km to NW — SE at greater depths (Fig. 10), this indicates that the shear-wave splitting direction

508 in WANT is dominated by anisotropy in the top 150 km of the mantle. In EANT, differences between SKS data and

509 predictions vary more. Measurements by Accardo et al. (2014) at stations located in the DML show good agreement

510 with our predictions, but measurements by Müller (2001) in that same region differ. At the GSM, the observations

511 are quasi-perpendicular to our predictions. Our predictions in Victoria Land are oriented grid NNW — SSE. Measure-

512 ments in this area present a lot of scatter and differences between studies. However, the general trend of the data in

513 northern Victoria Land is that the fast axis is grid NNE — SSW. In the southern part of the region, three measurements

514 by Pondrelli et al. (2006) are in closer agreement with our model predictions, but this is an area where our azimuthal

515 coverage is lower and the azimuthal anisotropy may not be resolved. These discrepancies between predictions and

516 measurements in EANT are likely due in part to differences in lateral resolution, but they may also point to deeper

517 anisotropy than our higher modes were able to detect and/or a crustal origin that we cannot resolve at the periods

518 analyzed. Zhou et al. (2023) showed indeed that azimuthal anisotropy is present in the crust, though they found that

519 its amplitude was relatively small. It may also indicate that the depth dependence of the anisotropy in EANT is even

520 more complex than can be resolved with the present data and higher resolution models will be needed to reconcile

521 the data sets.

6   Conclusions

We obtained a new three-dimensional model of shear-wave velocity and azimuthal anisotropy in the upper mantle and mantle transition zone under Antarctica. Our velocity model shows a clear east-west dichotomy with velocities faster than average down to at least 200 km in EANT and generally lower than average in WANT. In particular, the Marie Bird Land, which is located in the more tectonically active WANT and is associated with recent volcanism, is characterized by negative velocity anomalies down to about 400 km depth. This signal could thus be related to the presence of a plume, as suggested by other authors. However, while we found negative velocity perturbations between 50 km and 200 km as well as between 300 km and 400 km, it is unclear whether the two anomalies are connected and we thus cannot conclude regarding the existence of a plume with our data set. Using our velocity profiles to estimate the LAB depth, we estimate that the cratonic root is about 200 km thick and the LAB depth in the younger WANT is around 80 km.

We found significant azimuthal anisotropy in the top 300 km under the Antarctica continent and an abrupt change in the fast seismic wave direction was detected between East and West Antarctica, similar to the east-west dichotomy seen in the isotropic part of the model. The anisotropy amplitude is the strongest between 100 km and 200 km depth under East Antarctica, and depth changes in fast direction are observed within the craton. This suggests layering within the stable, old lithosphere, as seen in other regions of the world, and may reflect the history of formation of the craton.

Our model also enabled us to give new context to the origin of past shear-wave splitting measurements. Shear-wave splitting delay time predictions based on our anisotropy model show good agreement with observations in WANT where the dominant fast splitting direction is grid SW - NE. Considering that the anisotropy fast axis changes in our model from grid SW - NE in the top 150 km to roughly NW-SE at greater depths, this indicates that the shear-wave splitting direction in WANT is dominated by anisotropy in the top 150 km of the mantle. In EANT, however, less agreement between data and predictions was found, possibly indicating a more complex 3-D anisotropy than in WANT, associated with different stages of deformation during the assembly of the craton.

Acknowledgements

Data and code availability

The waveform and metadata used in this study were accessed through the GEOFON Program, hosted by the GFZ German Research Centre for Geosciences (https://www.gfz-potsdam.de/), and through the IRIS DMC, which is hosted by the Seismological Facilities for the Advancement of Geoscience (SAGE) (https://www.iris.edu/hq/sage). The following networks provided the data: UKNET (Brisbourne, A. et al., 2016), ASAIN (Istituto Nazionale di Oceanografia e di Geofisica Sperimentale, 1992), Australian National Seismograph Network (Geoscience Australia, 2021), AWI Network Antarctica (Alfred Wegener Institute For Polar And Marine Research (AWI), 1993), Chilean National Seismic Net-

work (https://www.fdsn.org/networks/detail/C/), Red Sismologica Nacional (Universidad de Chile, 2012), GEOSCOPE Institut de physique du globe de Paris (IPGP) and École et Observatoire des Sciences de la Terre de Strasbourg (EOST) (1982), GEOFON GEOFON Data Centre (1993), Global Telemetered Seismograph Network (Albuquerque Seismological Laboratory (ASL)/USGS, 1993), GSN (Scripps Institution of Oceanography, 1986; Albuquerque Seismological Laboratory/USGS, 2014), New Zealand National Seismograph Network (GNS Science, 2021), Pacific21 (https://www.fdsn.org/networks/detail/PS/), XD (Parker, T. and Beaudoin, B., 2007), SEARCH (https://www.fdsn.org/networks/detail/XJ_2004/), XH (Wiens, D. et al., 2014), Y3 (Russo, R., 2007), YJ (Russo, R., 2004), POLENET (Wiens and Nyblade, 2007b), TAMN-NET (Hansen, 2012), and GAMSEIS (Wiens and Nyblade, 2007a).

Obspy scripts were used to request and process the data (http://obspy.org). Earthquake source parameters were obtained from the Global CMT Project (www.globalcmt.org). The waveform modeling was performed using codes developed by Xu and Beghein (2019) and Xu et al. (2021). Software Mineos, which was used to calculate synthetic seismograms, was obtained through the CIG (https://geodynamics.org/resources/mineos). The transdimensional approach was based on the code of Bodin et al. (2012). Figures were made using Matplotlib (Hunter, 2007) and the Generic Mapping Code (https://www.generic-mapping-tools.org/). Models CRUST1.0 and 3D2018 were obtained from the IRIS EMC (http://ds.iris.edu/ds/products/emc).

Competing interests

The authors do not have any competing interests, financial or otherwise.

References

Accardo, N. J., Wiens, D. A., Hernandez, S., Aster, R. C., Nyblade, A., Huerta, A., Anandakrishnan, S., Wilson, T., Heeszel, D. S., and Dalziel, I. W. Upper mantle seismic anisotropy beneath the West Antarctic Rift System and surrounding region from shear wave splitting analysis. *Geophys. J. Int.*, 198(1):414–429, 2014. doi: 10.1093/gji/ggu117.

Albuquerque Seismological Laboratory (ASL)/USGS. Global Telemetered Seismograph Network (USAF/USGS), 1993.

Albuquerque Seismological Laboratory/USGS. Global Seismograph Network (GSN - IRIS/USGS), 2014.

Alfred Wegener Institute For Polar And Marine Research (AWI). AW – AWI Network Antarctica, 1993.

An, M., Wiens, D. A., Zhao, Y., Feng, M., Nyblade, A., Kanao, M., Li, Y., Maggi, A., and Lévêque, J.-J. Temperature, lithosphere-asthenosphere boundary, and heat flux beneath the Antarctic Plate inferred from seismic velocities. *J. Geophys. Res.: Solid Earth*, 120(12):8720–8742, 2015a. doi: 10.1002/2014JB011332.

An, M., Wiens, D. A., Zhao, Y., Feng, M., Nyblade, A. A., Kanao, M., Li, Y., Maggi, A., and Lévêque, J.-J. S-velocity model and inferred Moho topography beneath the Antarctic Plate from Rayleigh waves. *J. Geophys. Res.: Solid Earth*, 120(1):359–383, 2015b. doi: 10.1002/2014JB011332.

Anandakrishnan, S. and Wiens, D. A Broadband Seismic Investigation of Deep Continental Structure Across the East-West Antarctic Boundary, 2000.

Anderson, D. L. Love Wave Dispersion in Heterogeneous Anisotropic Media. *Geophysics*, 27:445–454, 1962. doi: 10.1190/1.1439042.

Anderson, J. B. *Antarctic marine geology*. Cambridge University Press, 1999. doi: 10.1017/CBO9780511759376.

Anderson, O. L., Schreiber, E., Liebermann, R. C., and Soga, N. Some elastic constant data on minerals relevant to geophysics. *Reviews of Geophysics*, 6(4):491–524, 1968.

Auer, L., Boschi, L., Becker, T. W., Nissen-Meyer, T., and Giardini, D. Savani: A variable resolution whole-mantle model of anisotropic shear velocity variations based on multiple data sets. *J. Geophys. Res.: Solid Earth*, 119(4):3006 – 3034, 2014. doi: 10.1002/2013jb010773.

Barklage, M., Wiens, D. A., Nyblade, A., and Anandakrishnan, S. Upper mantle seismic anisotropy of South Victoria Land and the Ross Sea coast, Antarctica from SKS and SKKS splitting analysis. *Geophys. J. Int.*, 178(2):729–741, 2009. doi: 10.1111/j.1365-246X.2009.04158.x.

Barruol, G. and Hoffmann, R. Upper mantle anisotropy beneath the Geoscope stations. *J. Geophys. Res.: Solid Earth*, 104(B5):10757–10773, 1999. doi: 10.1029/1999JB900033.

Bartzsch, S., Lebedev, S., and Meier, T. Resolving the lithosphere–asthenosphere boundary with seismic Rayleigh waves. *Geophysical Journal International*, 186(3):1152–1164, 2011.

Bayer, B., Müller, C., Eaton, D. W., and Jokat, W. Seismic anisotropy beneath Dronning Maud Land, Antarctica, revealed by shear wave splitting. *Geophys. J. Int.*, 171(1):339–351, 2007. doi: 10.1111/j.1365-246X.2007.03519.x.

Becker, T. W., Kellogg, J. B., Ekström, G., and O'Connell, R. J. Comparison of azimuthal seismic anisotropy from surface waves and finite strain from global mantle-circulation models. *Geophys. J. Int.*, 155(2):696 – 714, 2003. doi: 10.1046/j.1365-246x.2003.02085.x.

Beghein, C. Radial anisotropy and prior petrological constraints: A comparative study. *Journal of Geophysical Research*, 115(B03303), 2010. doi: 10.1029/2008jb005842.

Beghein, C., Yuan, K., Xing, Z., and Schmerr, N. Changes in Seismic Anisotropy Shed Light on the Nature of the Gutenberg Discontinuity. *Science*, 343(6176):1237 – 1240, 2014. doi: 10.1126/science.1246724.

Behrendt, J. C. Crustal and lithospheric structure of the West Antarctic Rift System from geophysical investigations—a review. *Global and Planetary Change*, 23(1-4):25–44, 1999.

Behrendt, J. C., LeMasurier, W. E., Cooper, A. K., Tessensohn, F., Tréhu, A., and Damaske, D. Geophysical studies of the West Antarctic Rift System. *Tectonics*, 10(6):1257–1273, 1991. doi: 10.1029/91tc00868.

Beucler, E., Stutzmann, E., and Montagner, J.-P. Surface wave higher-mode phase velocity measurements using a roller-coaster-type algorithm. *Geophys. J. Int.*, 155(1):289–307, 2003. doi: 10.1046/j.1365-246X.2003.02041.x.

Bevington, P. and Robinson, K. *Data Reduction and Error Analysis for the Physical Sciences*. McGraw-Hill, New York, N. Y., 3rd edition, 2002.

Birkey, A. and Ford, H. A. Anisotropic structure of the Australian continent. *Frontiers in Earth Science*, 10:1055480, 2023. doi: 10.3389/feart.2022.1055480.

Block, A. E., Bell, R. E., and Studinger, M. Antarctic crustal thickness from satellite gravity: Implications for the Transantarctic and Gamburtsev Subglacial Mountains. *Earth Planet. Sci. Lett.*, 288(1-2):194–203, 2009. doi: 10.1016/j.epsl.2009.09.022.

Bodin, T. and Sambridge, M. Seismic tomography with the reversible jump algorithm. *Geophysical Journal International*, 178(3):1411–1436, 2009.

Bodin, T., Sambridge, M., Tkalčić, H., Arroucau, P., Gallagher, K., and Rawlinson, N. Transdimensional inversion of receiver functions and surface wave dispersion. *Journal of Geophysical Research: Solid Earth*, 117(B2), 2012.

Bodin, T., Leiva, J., Romanowicz, B., Maupin, V., and Yuan, H. Imaging anisotropic layering with Bayesian inversion of multiple data types. *Geophysical Journal of the Royal Astronomical Society*, 206(1):605 – 629, 2016. doi: 10.1093/gji/ggw124.

Boger, S. D. Antarctica — Before and after Gondwana. *Gondwana Research*, 19(2):335–371, 2011. doi: https://doi.org/10.1016/j.gr.2010.09.003.

628 Brisbourne, A., Stuart, G., and O'Donnell, J.P. UKANET: UK Antarctic Network, 2016.

629 Chaput, J., Aster, R. C., Huerta, A., Sun, X., Lloyd, A., Wiens, D., Nyblade, A., Anandakrishnan, S., Winberry, J. P., and Wilson, T. The crustal
630   thickness of West Antarctica. *J. Geophys. Res.: Solid Earth*, 119(1):378–395, 2014. doi: 10.1002/2013JB010642.

631 Chen, X., Levin, V., Yuan, H., Klaser, M., and Li, Y. Seismic Anisotropic Layering in the Yilgarn and Superior Cratonic Lithosphere. *Journal of*
632   *Geophysical Research: Solid Earth*, 126(8):e2020JB021575, 2021. doi: 10.1029/2020JB021575.

633 Dahlen, F. The Normal Modes of a Rotating, Elliptical Earth. *Geophysical Journal of the Royal Astronomical Society*, 16(4):329 – 367, 1968.
634   doi: 10.1111/j.1365-246x.1968.tb00229.x.

635 Dalziel, I. W. D. Antarctica; a tale of two supercontinents? *Annu. Rev. Earth Planet. Sci.*, 20(1):501–526, 1992. doi: 10.1146/an-
636   nurev.ea.20.050192.002441.

637 Danesi, S. and Morelli, A. Group velocity of Rayleigh waves in the Antarctic region. *Physics of the Earth and Planetary Interiors*, 122(1-2):
638   55–66, 2000. doi: 10.1016/s0031-9201(00)00186-2.

639 Danesi, S. and Morelli, A. Structure of the upper mantle under the Antarctic Plate from surface wave tomography. *Geophys. Res. Lett.*, 28
640   (23):4395–4398, 2001. doi: 10.1029/2001GL013431.

641 Debayle, E. and Ricard, Y. Seismic observations of large-scale deformation at the bottom of fast-moving plates. *Earth and Planetary Science*
642   *Letters*, 376:165–177, 2013.

643 Debayle, E., Dubuffet, F., and Durand, S. An automatically updated S-wave model of the upper mantle and the depth extent of azimuthal
644   anisotropy. *Geophysical Research Letters*, 43(2):674–682, 2016.

645 DeMets, C., Gordon, R. G., Argus, D. F., and Stein, S. Effect of recent revisions to the geomagnetic reversal time scale on estimates of current
646   plate motions. *Geophys. Res. Lett.*, 21(20):2191–2194, 1994. doi: 10.1029/94GL02118.

647 Dewart, G. and Toksöz, M. N. Crustal Structure in East Antarctica from Surface Wave Dispersion. *Geophys. J. Int.*, 10(2):127–139, 1965.
648   doi: 10.1111/j.1365-246X.1965.tb03056.x.

649 Dziewonski, A. and Anderson, D. Preliminary reference Earth model. *Phys. Earth Planet. Inter.*, 25(4):297–356, 1981. doi: 10.1016/0031-
650   9201(81)90046-7.

651 Dziewonski, A. M., Chou, T.-A., and Woodhouse, J. H. Determination of earthquake source parameters from waveform data for studies of
652   global and regional seismicity. *J. Geophys. Res.: Solid Earth*, 86(B4):2825–2852, 1981. doi: 10.1029/JB086iB04p02825.

653 Ebbing, J., Dilixiati, Y., and Haas, P. e. a. East Antarctica magnetically linked to its ancient neighbours. *Scientific Reports*, 11(5513), 2021.
654   doi: 10.1038/s41598-021-84834-1.

655 Ekström, G. and Dziewonski, A. M. The unique anisotropy of the Pacific upper mantle. *Nature*, 394:168 – 172, 07 1998. doi: 10.1038/28148.

656 Ekström, G., Nettles, M., and Dziewoński, A. M. The global CMT project 2004–2010: Centroid-moment tensors for 13,017 earthquakes. *Phys.*
657   *Earth Planet. Inter.*, 200-201:1–9, 2012. doi: 10.1016/j.pepi.2012.04.002.

658 Emry, E., Nyblade, A. A., Julià, J., Anandakrishnan, S., Aster, R., Wiens, D. A., Huerta, A. D., and Wilson, T. J. The mantle transition zone
659   beneath West Antarctica: Seismic evidence for hydration and thermal upwellings. *Geochem. Geophys. Geosystems*, 16(1):40–58, 2015.
660   doi: 10.1002/2014GC005588.

661 Emry, E. L., Nyblade, A. A., Horton, A., Hansen, S. E., Julià, J., Aster, R. C., Huerta, A. D., Winberry, J. P., Wiens, D. A., and Wilson, T. J.
662   Prominent thermal anomalies in the mantle transition zone beneath the Transantarctic Mountains. *Geology*, 48(7):748–752, 2020.
663   doi: 10.1130/g47346.1.

664 Evison, F., Ingham, C., Orr, R., and le Fort, J. Thickness of the Earth's crust in Antarctica and the surrounding oceans. *Geophys. J. R. A. S.*, 3
665   (3):289–306, 1960. doi: 10.1111/j.1365-246X.1960.tb01704.x.

666 Ferraccioli, F., Finn, C. A., Jordan, T. A., Bell, R. E., Anderson, L. M., and Damaske, D. East Antarctic rifting triggers uplift of the Gamburtsev
667   Mountains. *Nature*, 479(7373):388–392, 2011. doi: 10.1038/nature10566.

668 Ferreira, A. M., Faccenda, M., Sturgeon, W., Chang, S.-J., and Schardong, L. Ubiquitous lower-mantle anisotropy beneath subduction zones.
669   *Nature Geoscience*, pages 1 – 8, 2019. doi: 10.1038/s41561-019-0325-7.

670 Finotello, M., Nyblade, A., Julia, J., Wiens, D., and Anandakrishnan, S. Crustal Vp-Vs ratios and thickness for Ross Island and the Transantarc-
671   tic Mountain front, Antarctica. *Geophys. J. Int.*, 185(1):85–92, 2011. doi: 10.1111/j.1365-246x.2011.04946.x.

672 Fitzgerald, P. *Tectonics and landscape evolution of the Antarctic plate since Gondwana breakup, with an emphasis on the West Antarctic rift*
673   *system and the Transantarctic Mountains*, volume 35, pages 453–469. The Royal Society of New Zealand, New Zealand, 2002.

674 Foster, K., Dueker, K., Schmandt, B., and Yuan, H. A sharp cratonic lithosphere–asthenosphere boundary beneath the American Midwest
675   and its relation to mantle flow. *Earth and Planetary Science Letters*, 402(C):82 – 89, 2014. doi: 10.1016/j.epsl.2013.11.018.

676 Fouch, M. J. and Fischer, K. M. Mantle anisotropy beneath northwest Pacific subduction zones. *J. Geophys. Res.: Solid Earth*, 101(B7):15987,
677   1996. doi: 10.1029/96jb00881.

678 GEOFON Data Centre. GEOFON Seismic Network, 1993.

679 Geoscience Australia. Australian National Seismograph Network Data Collection, 2021.

680 GNS Science. GeoNet Aotearoa New Zealand Seismic Digital Waveform Dataset, 2021.

681 Granot, R., Cande, S., Stock, J., Davey, F., and Clayton, R. Postspreading rifting in the Adare Basin, Antarctica: regional tectonic conse-
682   quences. *Geochem. Geophys. Geosystems*, 11(8), 2010. doi: 10.1029/2010GC003105.

683 Graw, J. H. and Hansen, S. E. Upper mantle seismic anisotropy beneath the Northern Transantarctic Mountains, Antarctica from PKS, SKS,
684   and SKKS splitting analysis. *Geochemistry, Geophysics, Geosystems*, 18(2):544–557, 2017. doi: 10.1002/2016gc006729.

685 Gripp, A. E. and Gordon, R. G. Young tracks of hotspots and current plate velocities. *Geophys. J. Int.*, 150(2):321–361, 2002.

686 Gung, Y., Panning, M. P., and Romanowicz, B. Global anisotropy and the thickness of continents. *Nature*, 422(6933):707 – 711, 2003.
687   doi: 10.1038/nature01559.

688 Hansen, P. C. *Rank-deficient and discrete ill-posed problems: numerical aspects of linear inversion*. SIAM, 1998.

689 Hansen, S. Transantarctic Mountains Northern Network, 2012.

690 Hansen, S. E., Julia, J., Nyblade, A. A., Pyle, M. L., Wiens, D. A., and Anandakrishnan, S. Using S wave receiver functions to estimate crustal
691   structure beneath ice sheets: An application to the Transantarctic Mountains and East Antarctic craton. *Geochem. Geophys. Geosystems*,
692   10(8), 2009. doi: 10.1029/2009GC002576.

693 Hansen, S. E., Nyblade, A. A., Heeszel, D. S., Wiens, D. A., Shore, P., and Kanao, M. Crustal structure of the Gamburtsev Mountains,
694   East Antarctica, from S-wave receiver functions and Rayleigh wave phase velocities. *Earth Planet. Sci. Lett.*, 300(3-4):395–401, 2010.
695   doi: 10.1016/j.epsl.2010.10.022.

696 Hansen, S. E., Graw, J. H., Kenyon, L. M., Nyblade, A. A., Wiens, D. A., Aster, R. C., Huerta, A. D., Anandakrishnan, S., and Wilson, T. Imaging the
697   Antarctic mantle using adaptively parameterized P-wave tomography: Evidence for heterogeneous structure beneath West Antarctica.
698   *Earth Planet. Sci. Lett.*, 408:66–78, 2014. doi: 10.1016/j.epsl.2014.09.043.

699 Heeszel, D. S., Wiens, D. A., Nyblade, A. A., Hansen, S. E., Kanao, M., An, M., and Zhao, Y. Rayleigh wave constraints on the structure
700   and tectonic history of the Gamburtsev Subglacial Mountains, East Antarctica. *J. Geophys. Res.: Solid Earth*, 118(5):2138–2153, 2013.
701   doi: 10.1002/jgrb.50171.

702 Heeszel, D. S., Wiens, D. A., Anandakrishnan, S., Aster, R. C., Dalziel, I. W. D., Huerta, A. D., Nyblade, A. A., Wilson, T. J., and Winberry, J. P.

703   Upper mantle structure of central and West Antarctica from array analysis of Rayleigh wave phase velocities. *J. Geophys. Res.: Solid Earth*,
704   121(3):1758–1775, 2016. doi: 10.1002/2015jb012616.

705   Hernandez, S., Wiens, D., Anandakrishnan, S., Aster, R., Huerta, A., Nyblade, A., and Wilson, T. Seismic anisotropy of the Antarctic upper
706   mantle from shear wave splitting analysis of POLENET and AGAP seismograms. In *AGU Fall Meeting Abstracts*, volume 2009, pages U51C–
707   0043, 2009.

708   Huang, Q., Schmerr, N., Waszek, L., and Beghein, C. Constraints on Seismic Anisotropy in the Mantle Transition Zone From Long-Period SS
709   Precursors. *J. Geophys. Res.: Solid Earth*, 124(7):6779–6800, 6 2019. doi: 10.1029/2019jb017307.

710   Hunter, J. D. Matplotlib: A 2D Graphics Environment. *Computing in Science Engineering*, 9(3):90–95, 2007. doi: 10.1109/MCSE.2007.55.

711   Institut de physique du globe de Paris (IPGP) and École et Observatoire des Sciences de la Terre de Strasbourg (EOST). GEOSCOPE, French
712   Global Network of broad band seismic stations, 1982.

713   Istituto Nazionale di Oceanografia e di Geofisica Sperimentale. Antarctic Seismographic Argentinean Italian Network - ASAIN, 1992.

714   Jeans, J. H. The propagation of earthquake waves. *Proceedings of the Royal Society of London. Series A, Containing Papers of a Mathematical*
715   *and Physical Character*, 102(718):554–574, 1923. doi: 10.1098/rspa.1923.0015.

716   Karato, S.-i. and Wu, P. Rheology of the Upper Mantle - a Synthesis. *Science*, 260(5109):771 – 778, 05 1993. doi: 10.1126/science.260.5109.771.

717   Karato, S.-i., Jung, H., Katayama, I., Skemer, P., and Skemer, P. Geodynamic Significance of Seismic Anisotropy of the Upper Mantle: New
718   Insights from Laboratory Studies. *Annu. Rev. Earth Planet. Sci.*, 36(1):59 – 95, 2008. doi: 10.1146/annurev.earth.36.031207.124120.

719   Kovach, R. and Press, F. Surface wave dispersion and crustal structure in Antarctica and the Surrounding Oceans. *Ann. Geophys.*, 14:211–224,
720   1961. doi: 10.4401/ag-5296.

721   Laske, G., Masters, G., Ma, Z., and Pasyanos, M. Update on CRUST1. 0—A 1-degree global model of Earth's crust. In *Geophys. res. abstr*,
722   volume 15, page 2658, 2013.

723   Lawrence, J. F., Wiens, D. A., Nyblade, A. A., Anandakrishnan, S., Shore, P. J., and Voigt, D. Crust and upper mantle structure of the
724   Transantarctic Mountains and surrounding regions from receiver functions, surface waves, and gravity: Implications for uplift models.
725   *Geochem. Geophys. Geosystems*, 7(10):n/a – n/a, 2006. doi: 10.1029/2006gc001282.

726   Lebedev, S., Nolet, G., Meier, T., and Van der Hilst, R. D. Automated multimode inversion of surface and S waveforms. *Geophys. J. Int.*, 162
727   (3):951–964, 2005. doi: 10.1111/j.1365-246X.2005.02708.x.

728   LeMasurier, W. E. and Landis, C. A. Mantle-plume activity recorded by low-relief erosion surfaces in West Antarctica and New Zealand. *GSA*
729   *Bulletin*, 108(11):1450–1466, 1996. doi: 10.1130/0016-7606(1996)108<1450:mparbl>2.3.co;2.

730   Lloyd, A., Wiens, D., Zhu, H., Tromp, J., Nyblade, A., Aster, R., Hansen, S., Dalziel, I., Wilson, T., Ivins, E., and O'Donnell, J. P. Seismic structure
731   of the Antarctic upper mantle imaged with adjoint tomography. *J. Geophys. Res.: Solid Earth*, 125(3), 2020. doi: 10.1029/2019JB017823.

732   Lloyd, A. J., Wiens, D. A., Nyblade, A. A., Anandakrishnan, S., Aster, R. C., Huerta, A. D., Wilson, T. J., Dalziel, I. W., Shore, P. J., and Zhao, D.
733   A seismic transect across West Antarctica: Evidence for mantle thermal anomalies beneath the Bentley Subglacial Trench and the Marie
734   Byrd Land Dome. *J. Geophys. Res.: Solid Earth*, 120(12):8439–8460, 2015. doi: 10.1002/2015JB012455.

735   Long, M. D. and van der Hilst, R. D. Upper mantle anisotropy beneath Japan from shear wave splitting. *Phys. Earth Planet. Inter.*, 151(3-4):
736   206–222, 2005. doi: 10.1016/j.pepi.2005.03.003.

737   Lucas, E. M., Nyblade, A. A., Accardo, N. J., Lloyd, A. J., Wiens, D. A., Aster, R. C., Wilson, T. J., Dalziel, I. W., Stuart, G. W., O'Donnell, J. P.,
738   Winberry, J. P., and Huerta, A. D. Shear Wave Splitting Across Antarctica: Implications for Upper Mantle Seismic Anisotropy. *Journal of*
739   *Geophysical Research: Solid Earth*, 127(4), 2022. doi: 10.1029/2021jb023325.

740   Lynner, C. and Long, M. D. Heterogeneous seismic anisotropy in the transition zone and uppermost lower mantle: evidence from South

America, Izu-Bonin and Japan. *Geophys. J. R. A. S.*, 201(3):1545 – 1552, 2015. doi: 10.1093/gji/ggv099.

Lynner, C., Lynner, C., and Long, M. D. Lowermost mantle anisotropy and deformation along the boundary of the African LLSVP. *Geophys. Res. Lett.*, 41:3447–3454, 2014. doi: 10.1002/2014gl059875.

Marone, F., Gung, Y., and Romanowicz, B. Three-dimensional radial anisotropic structure of the North American upper mantle from inversion of surface waveform data. *Geophys. J. R. A. S.*, 171(1):206 – 222, 2007. doi: 10.1111/j.1365-246x.2007.03465.x.

Masters, G., Woodhouse, J., and Freeman, G. Mineos v1.0.2 [software], 2011.

Meier, U., Trampert, J., and Curtis, A. Global variations of temperature and water content in the mantle transition zone from higher mode surface waves. *Earth and Planetary Science Letters*, 282(1-4):91 – 101, 2009. doi: 10.1016/j.epsl.2009.03.004.

Montagner, J.-P. and Jobert, N. Vectorial tomography ii. Application to the Indian Ocean. *Geophysical Journal of the Royal Astronomical Society*, 94(2):309–344, 1988. doi: 10.1111/j.1365-246x.1988.tb05904.x.

Montagner, J.-P. and Nataf, H. A Simple Method for Inverting the Azimuthal Anisotropy of Surface-Waves. *J. Geophys. Res.*, 91(B1):511 – 520, 1986. doi: 10.1029/jb091ib01p00511.

Montagner, J. P., Romanowicz, B., and Karczewski, J.-F. A first step toward an oceanic geophysical observatory. *Eos, Transactions American Geophysical Union*, 75(13):150–154, 1994. doi: 10.1029/94EO00848.

Montagner, J.-P., Griot-Pommera, D.-A., and Lavé, J. How to relate body wave and surface wave anisotropy? *Journal of Geophysical Research: Solid Earth*, 105(B8):19015–19027, 2000.

Morelli, A. and Danesi, S. Seismological imaging of the Antarctic continental lithosphere: a review. *Global and Planetary Change*, 42(1): 155–165, 2004. doi: https://doi.org/10.1016/j.gloplacha.2003.12.005.

Müller, C. Upper mantle seismic anisotropy beneath Antarctica and the Scotia Sea region. *Geophys. J. Int.*, 147(1):105–122, 2001. doi: 10.1046/j.1365-246X.2001.00517.x.

O'Donnell, J., Brisbourne, A. M., Stuart, G., Dunham, C., Yang, Y., Nield, G., Whitehouse, P., Nyblade, A., Wiens, D., Anandakrishnan, S., Aster, R. C., Huerta, A. D., Lloyd, A. J., Wilson, T., and Winberry, J. P. Mapping crustal shear wave velocity structure and radial anisotropy beneath West Antarctica using seismic ambient noise. *Geochem. Geophys. Geosystems*, 20(11):5014–5037, 2019. doi: 10.1029/2019GC008459.

Paige, C. C. and Saunders, M. A. LSQR: An algorithm for sparse linear equations and sparse least squares. *ACM Transactions on Mathematical Software (TOMS)*, 8(1):43–71, 1982.

Panning, M. and Romanowicz, B. A three-dimensional radially anisotropic model of shear velocity in the whole mantle. *Geophys. J. Int.*, 167(1):361 – 379, 2006. doi: 10.1111/j.1365-246x.2006.03100.x.

Parker, T. and Beaudoin, B. Development of A Power and Communication for Remote Autonomous GPS and Seismic Stations in Antarctica, 2007.

Pondrelli, S. and Azzara, R. Upper mantle anisotropy in Victoria Land (Antarctica). In *Geodynamics of Lithosphere & Earth's Mantle*, pages 433–442. Springer, 1998.

Pondrelli, S., Margheriti, L., and Danesi, S. Antarctica, Contributions to Global Earth Sciences. pages 155–161, 2006. doi: 10.1007/3-540-32934-x_19.

Press, F. and Gilbert, D. Extent of the Antarctic Continent. *Science*, 129(3347):462–463, 1959. doi: 10.1126/science.129.3347.462.

Pyle, M. L., Wiens, D. A., Nyblade, A. A., and Anandakrishnan, S. Crustal structure of the Transantarctic Mountains near the Ross Sea from ambient seismic noise tomography. *Journal of Geophysical Research: Solid Earth*, 115(B11), 2010. doi: 10.1029/2009jb007081.

Ramirez, C., Nyblade, A., Hansen, S., Wiens, D., Anandakrishnan, S., Aster, R., Huerta, A., Shore, P., and Wilson, T. Crustal and upper-mantle

778   structure beneath ice-covered regions in Antarctica from S-wave receiver functions and implications for heat flow. *Geophysical Journal*
779   *International*, 204(3):1636–1648, 2016. doi: 10.1093/gji/ggv542.

780   Ramirez, C., Nyblade, A., Emry, E. L., Julià, J., Sun, X., Anandakrishnan, S., Wiens, D. A., Aster, R. C., Huerta, A. D., Winberry, P., and Wilson,
781   T. Crustal structure of the Transantarctic Mountains, Ellsworth Mountains and Marie Byrd Land, Antarctica: constraints on shear wave
782   velocities, Poisson's ratios and Moho depths. *Geophysical Journal International*, 211(3):1328–1340, 2017. doi: 10.1093/gji/ggx333.

783   Reading, A. M. and Heintz, M. Seismic anisotropy of East Antarctica from shear-wave splitting: Spatially varying contributions from litho-
784   spheric structural fabric and mantle flow? *Earth Planet. Sci. Lett.*, 268(3-4):433–443, 2008. doi: 10.1016/j.epsl.2008.01.041.

785   Ritzwoller, M. H., Shapiro, N. M., Levshin, A. L., and Leahy, G. M. Crustal and upper mantle structure beneath Antarctica and surrounding
786   oceans. *J. Geophys. Res.: Solid Earth*, 106(B12):30645–30670, 2001. doi: 10.1029/2001JB000179.

787   Roult, G., Rouland, D., and Montagner, J. Antarctica II: Upper-mantle structure from velocities and anisotropy. *Phys. Earth Planet. Inter.*, 84
788   (1-4):33–57, 1994. doi: 10.1016/0031-9201(94)90033-7.

789   Russo, R. Studies of crust and upper mantle structure, mantle flow and geodynamics of the Chile Ridge subduction zone, 2004.

790   Russo, R. Studies of crust and upper mantle structure, mantle flow and geodynamics of the Chile Ridge subduction zone, 2007.

791   Salimbeni, S., Pondrelli, S., Danesi, S., and Morelli, A. Seismic anisotropy of the Victoria Land region, Antarctica. *Geophysical Journal*
792   *International*, 182(1):421–432, 2010. doi: 10.1111/j.1365-246x.2010.04624.x.

793   Savage, M. K. Seismic anisotropy and mantle deformation: What have we learned from shear wave splitting? *Reviews of Geophysics*, 37(1):
794   65 – 106, 1999. doi: 10.1029/98rg02075.

795   Scripps Institution of Oceanography. Global Seismograph Network - IRIS/IDA, 1986.

796   Shen, W., Wiens, D. A., Anandakrishnan, S., Aster, R. C., Gerstoft, P., Bromirski, P. D., Hansen, S. E., Dalziel, I. W., Heeszel, D. S., Huerta,
797   A. D., Nyblade, A. A., Stephen, R., Wilson, T. J., and Winberry, J. P. The crust and upper mantle structure of central and West
798   Antarctica from Bayesian inversion of Rayleigh wave and receiver functions. *J. Geophys. Res.: Solid Earth*, 123(9):7824–7849, 2018.
799   doi: 10.1029/2017JB015346.

800   Sieminski, A., Debayle, E., and Lévêque, J.-J. Seismic evidence for deep low-velocity anomalies in the transition zone beneath West Antarc-
801   tica. *Earth Planet. Sci. Lett.*, 216(4):645–661, 2003. doi: 10.1016/S0012-821X(03)00518-1.

802   Silver, P. G. Seismic anisotropy beneath the continents: Probing the depths of geology. *Annu. Rev. Earth Planet. Sci.*, 24, 1996.
803   doi: 10.1146/annurev.earth.24.1.385.

804   Silver, P. G. and Chan, W. W. Implications for continental structure and evolution from seismic anisotropy. *Nature*, 335(6185):34–39, 1988.
805   doi: 10.1038/335034a0.

806   Smith, D. B., Ritzwoller, M. H., and Shapiro, N. M. Stratification of anisotropy in the Pacific upper mantle. *J. Geophys. Res.*, 109(B11):243 –
807   22, 2004. doi: 10.1029/2004jb003200.

808   Snyder, D. and Bruneton, M. Seismic anisotropy of the Slave craton, NW Canada, from joint interpretation of SKS and Rayleigh waves.
809   *Geophysical Journal International*, 169(1):170–188, 04 2007. doi: 10.1111/j.1365-246X.2006.03287.x.

810   Stutzmann, E. and Montagner, J.-P. An inverse technique for retrieving higher mode phase velocity and mantle structure. *Geophys. J. Int.*,
811   113(3):669–683, 1993. doi: 10.1111/j.1365-246X.1993.tb04659.x.

812   Tozer, B., Sandwell, D. T., Smith, W. H., Olson, C., Beale, J., and Wessel, P. Global bathymetry and topography at 15 arc sec: SRTM15+. *Earth*
813   *Space Sci.*, 6(10):1847–1864, 2019. doi: 10.1029/2019EA000658.

814   Trampert, J. and van Heijst, H. J. Global azimuthal anisotropy in the transition zone. *Science*, 296(5571):1297–1299, 2002.
815   doi: 10.1126/science.1070264.

816 Trampert, J. and Woodhouse, J. H. Global anisotropic phase velocity maps for fundamental mode surface waves between 40 and 150 s.
817 *Geophys. J. Int.*, 154(1):154–165, 2003. doi: 10.1046/j.1365-246X.2003.01952.x.

818 Universidad de Chile. Red Sismologica Nacional, 2012.

819 Visser, K. *Monte Carlo search techniques applied to the measurement of higher mode phase velocities and anisotropic surface wave tomog-*
820 *raphy. Geologica Ultraiectina (285)*. Departement Aardwetenschappen, 2008. OCLC: 6893359236.

821 Visser, K., Lebedev, S., Trampert, J., and Kennett, B. Global Love wave overtone measurements. *Geophysical Research Letters*, 34(3), 2007.

822 Volk, O., White, R. S., Pilia, S., Green, R. G., Maclennan, J., and Rawlinson, N. Oceanic crustal flow in Iceland observed using seismic
823 anisotropy. *Nature Geoscience*, 14(3):168–173, 2021. doi: 10.1038/s41561-021-00702-7.

824 Watson, T., Nyblade, A., Wiens, D. A., Anandakrishnan, S., Benoit, M., Shore, P. J., Voigt, D., and VanDecar, J. P and S velocity structure of the
825 upper mantle beneath the Transantarctic Mountains, East Antarctic craton, and Ross Sea from travel time tomography. *Geochemistry,*
826 *Geophysics, Geosystems*, 7(7), 2006. doi: 10.1029/2005gc001238.

827 Wiens, D. and Nyblade, A. A Broadband Seismic Experiment to Image the Lithosphere beneath the Gamburtsev Mountains, East Antarctica,
828 2007a.

829 Wiens, D. and Nyblade, A. IPY POLENET-Antarctica: Investigating links between geodynamics and ice sheets, 2007b.

830 Wiens, D., Aster, R., and Bromirski, P. Collaborative Research: Collaborative Research: Dynamic Response of the Ross Ice Shelf to Ocean
831 Waves and Structure and Dynamics of the Ross Sea from a Passive Seismic Deployment on the Ross Ice Shelf, 2014.

832 Winberry, J. P. and Anandakrishnan, S. Crustal structure of the West Antarctic rift system and Marie Byrd Land hotspot. *Geology*, 32(11):
833 977–980, 2004. doi: 10.1130/g20768.1.

834 Wirth, E. A. and Long, M. D. A contrast in anisotropy across mid-lithospheric discontinuities beneath the central United States—A relic of
835 craton formation. *Geology*, 42(10):851–854, 2014. doi: 10.1130/g35804.1.

836 Woodhouse, J. The coupling and attenuation of nearly resonant multiplets in the Earth's free oscillation spectrum. *Geophysical Journal of*
837 *the Royal Astronomical Society*, 61(2):261 – 283, 1980. doi: 10.1111/j.1365-246x.1980.tb04317.x.

838 Wörner, G. Lithospheric dynamics and mantle sources of alkaline magmatism of the Cenozoic West Antarctic Rift System. *Global and*
839 *Planetary Change*, 23(1-4):61–77, 1999. doi: 10.1016/S0921-8181(99)00051-X.

840 Xu, H. and Beghein, C. Measuring higher mode surface wave dispersion using a transdimensional Bayesian approach. *Geophys. J. Int.*, 218
841 (1):333–353, 2019. doi: 10.1093/gji/ggz133.

842 Xu, H., Beghein, C., Panning, M., Drilleau, M., Lognonné, P., van Driel, M., Ceylan, S., Böse, M., Brinkman, N., Clinton, J., et al. Measuring
843 fundamental and higher mode surface wave dispersion on Mars from seismic waveforms. *Earth Space Sci.*, 8(2):e2020EA001263, 2021.
844 doi: 10.1029/2020EA001263.

845 Yoshizawa, K. and Ekström, G. Automated multimode phase speed measurements for high-resolution regional-scale tomography: appli-
846 cation to North America. *Geophysical Journal International*, 183(3):1538–1558, 2010.

847 Yoshizawa, K. and Kennett, B. Non-linear waveform inversion for surface waves with a neighbourhood algorithm—application to multimode
848 dispersion measurements. *Geophysical Journal International*, 149(1):118–133, 2002.

849 Yoshizawa, K. and Kennett, B. Multimode surface wave tomography for the Australian region using a three-stage approach incorporating
850 finite frequency effects. *J. Geophys. Res.: Solid Earth*, 109(B2), 2004. doi: 10.1029/2002JB002254.

851 Yuan, H. and Romanowicz, B. Lithospheric layering in the North American craton. *Nature*, 466(7310):1063–1068, 2010.

852 Yuan, H., Romanowicz, B., Fischer, K. M., and Abt, D. L. 3-D shear wave radially and azimuthally anisotropic velocity model of the

North American upper mantle. *Geophysical Journal of the Royal Astronomical Society*, 184(3):1237 – 1260, 2011. doi: 10.1111/j.1365-246x.2010.04901.x.

Yuan, K. and Beghein, C. Seismic anisotropy changes across upper mantle phase transitions. *Earth Planet. Sci. Lett.*, 374:132–144, 2013.

Yuan, K. and Beghein, C. Three-dimensional variations in Love and Rayleigh wave azimuthal anisotropy for the upper 800 km of the mantle. *J. Geophys. Res.: Solid Earth*, 119(4):3232–3255, 2014.

Zhang, H., Zhao, D., Ju, C., Li, Y. E., Li, G., Ding, M., Chen, S., and Zhao, J. Upper Mantle Deformation of the Terror Rift and Northern Transantarctic Mountains in Antarctica: Insight From P Wave Anisotropic Tomography. *Geophys. Res. Lett.*, 47(9), 2020. doi: 10.1029/2019gl086511.

Zhou, Z., Wiens, D. A., Shen, W., Aster, R. C., Nyblade, A., and Wilson, T. J. Radial Anisotropy and Sediment Thickness of West and Central Antarctica Estimated From Rayleigh and Love Wave Velocities. *Journal of Geophysical Research: Solid Earth*, 127(3), 2022. doi: 10.1029/2021jb022857.

Zhou, Z., Wiens, D. A., Nyblade, A., Aster, R. C., Wilson, T. J., and Shen, W. Crustal and Uppermost Mantle Azimuthal Seismic Anisotropy of Antarctica from Ambient Noise Tomography. *Journal of Geophysical Research: Solid Earth*, 2023. submitted.
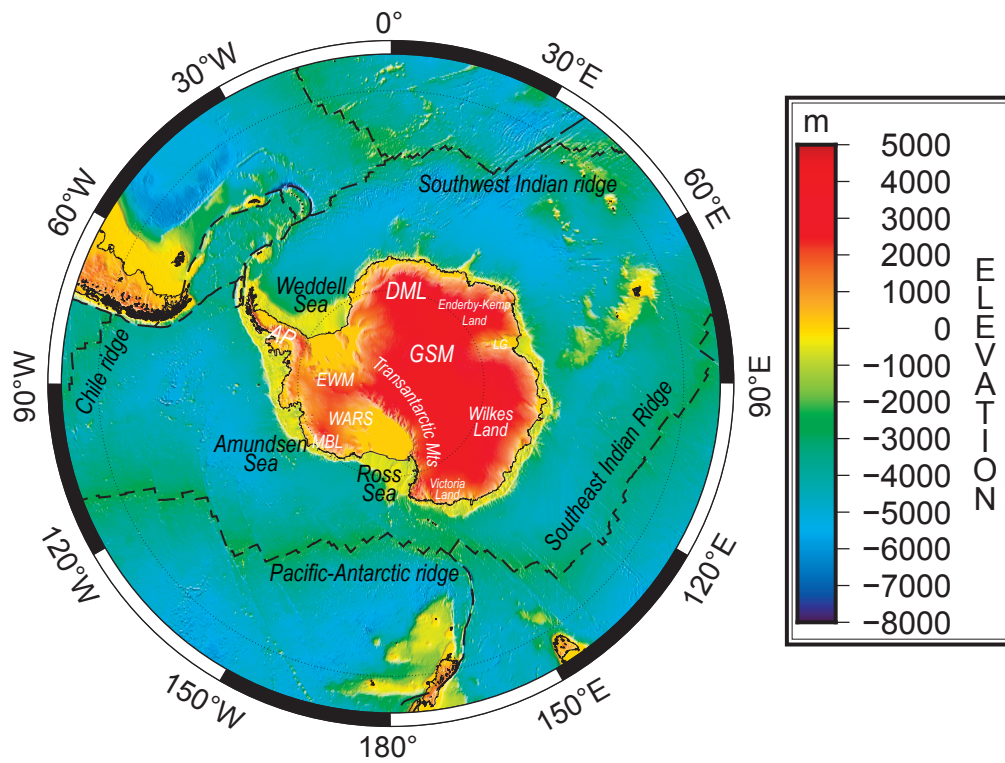
Figure 1 Topographic and bathymetric map of Antarctica and surrounding areas based on model SRTM15+ (Tozer et al., 2019). AP = Antarctica Peninsula; DML = Dronning Maud Land; EWM = Ellsworth-Whitmore Mountains; GSM = Gamburtsev Subglacial Mountains; LG = Lambert Graben; WARS = West Antarctic rift system. Ocean ridges are indicated by the dashed lines.
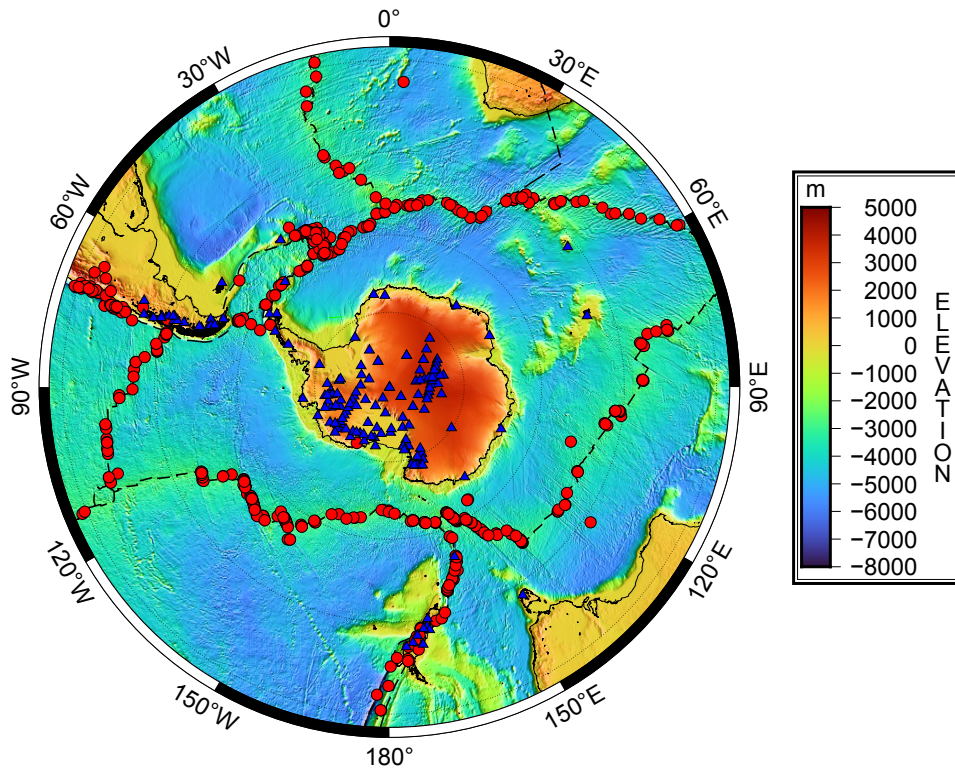
Figure 2 Maps of the selected event location (red circles) and stations (blue triangles) superimposed to bathymetry and topography (Tozer et al., 2019). Ocean ridges are shown by the dashed black lines.
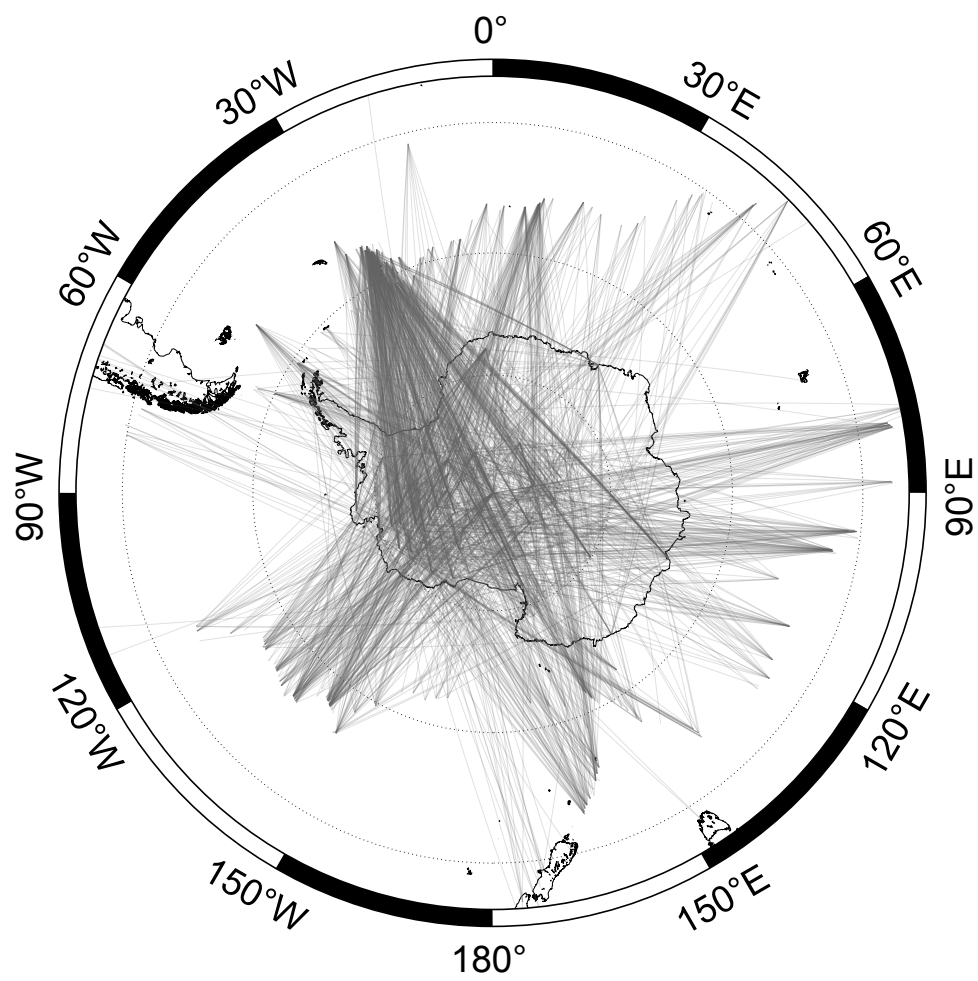
Figure 3 Ray-path coverage of all event-station pairs which passed all quality control steps.
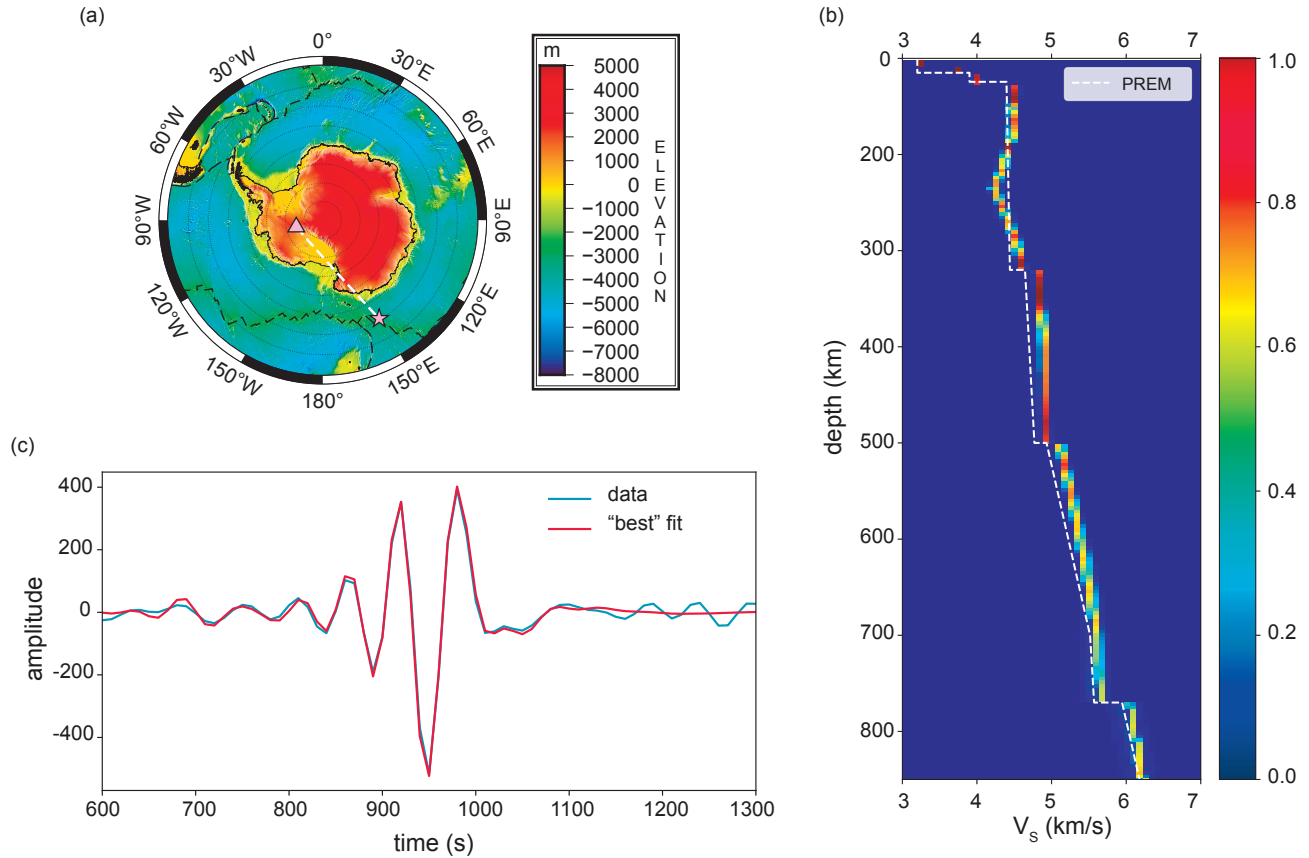
Figure 4 Illustration of the MCMC method employed. (a) Topographic map of Antarctica with selected station (triangle) and event (star). Plate boundaries are shown by the dashed black lines. (b) The resulting distribution of velocity models between the selected event-station pair. The color scale represents the likelihood of the model at a given depth. PREM is shown for reference. (c) Waveform fit for one of the best-fitting models.

Table 1 Selection of frequency-time windows. The first and second window indices correspond to the fundamental mode and the third window is for higher modes. The first and third windows share the same start time, which is determined by the S- or SS-wave arrival times. All other start/end times are determined by Δ/U, where Δ is the event epicentral distance and the values of the group velocities U are indicated in the table.

Window index	Frequency(mHz)	Start	End
1	5-10	S or SS	$U = 2.95\ km/s$
2	10-20	$U = 4.30\ km/s$	$U = 3.20\ km/s$
3	10-20	S or SS	$U = 4.30\ km/s$

Table 2 Significance of 2Ψ and 4Ψ terms at different depths from F-test analysis. A lower probability means that the model with more parameters has significantly lower misfits compared to the model with fewer parameters, and thus those extra parameters are needed to explain the data.

Depth	P(iso + 2Ψ == iso)	P(iso + 2Ψ + 4Ψ == iso + 2Ψ)
60 km	0.23%	6.62%
150 km	4.40%	37.50%
200 km	2.98%	35.41%
250 km	12.56%	39.50%
350 km	15.19%	30.09%
450 km	19.67%	44.74%
600 km	34.21%	25.54%
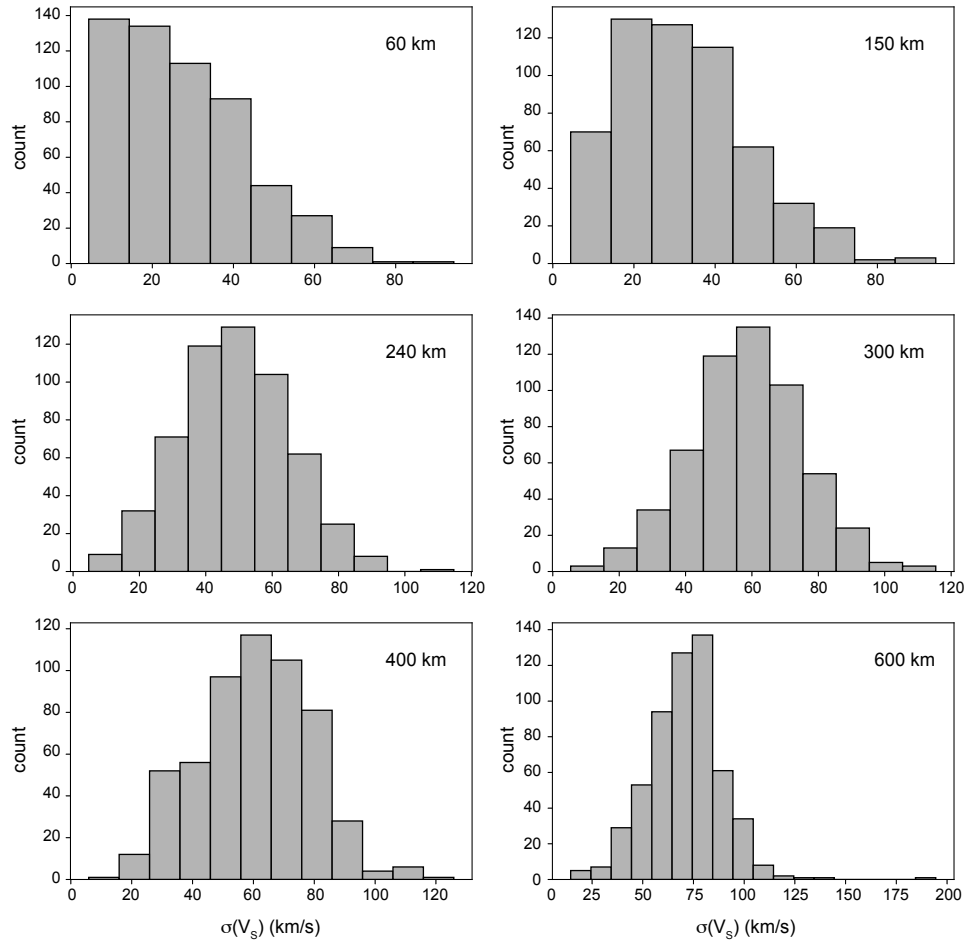
Figure 5 Distribution of path-averaged velocity $V_{SV}(z)$ standard deviations at different depths. All paths shown in Fig. 3 were included, and the standard deviation for each path is calculated from the ensemble of models obtained by our MCMC algorithm.
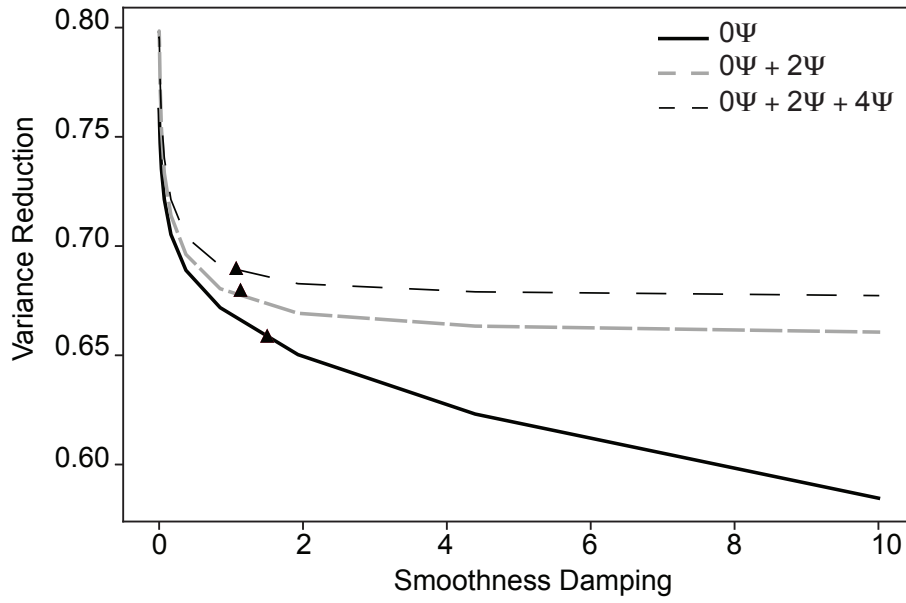
Figure 6   Example of damping parameter selection based on the L-curve method. The optimal damping parameters are selected at the elbow of the curves and are denoted by triangles. We first searched for the damping parameters for the 0Ψ-term. The $0\Psi + 2\Psi$ curve was obtained by fixing the selected isotropic damping parameter and changing the 2Ψ-term damping. The $0\Psi + 2\Psi + 4\Psi$ curve resulted from varying the 4Ψ damping parameter while fixing the isotropic and 2Ψ-term damping parameters.
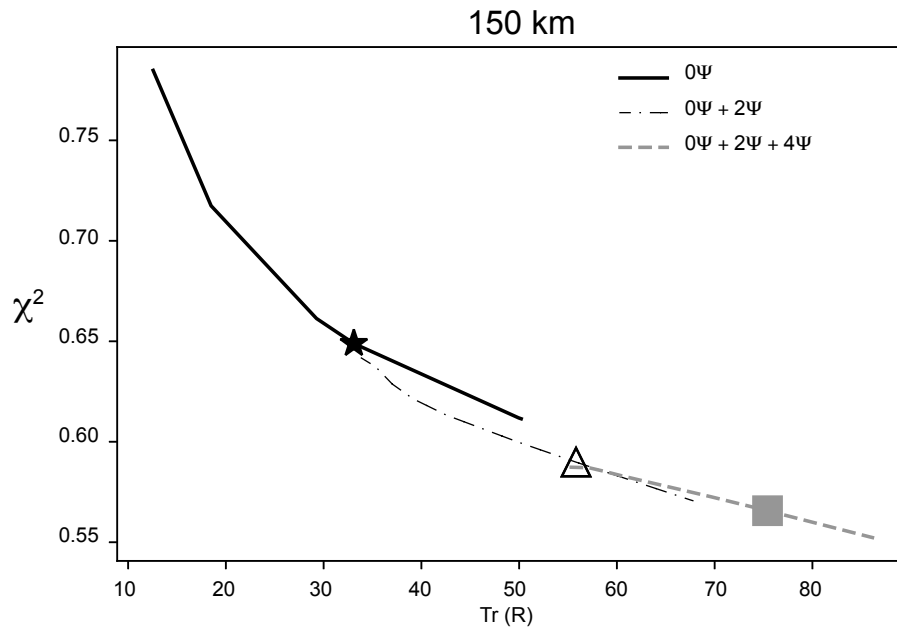

Figure 7   Example of reduced χ^2 as a function of the trace of the resolution matrix $\mathbf{R}$ for inversions at 150 km depth. The solid black curve is for inversions of the isotropic terms only. Different values of the trace of the resolution matrix were obtained by applying different levels of damping. The preferred model selected by the L-curve method is marked by the black star. The thin black curve represents the inversion with both isotropic and 2Ψ terms with fixed isotropic damping parameter (corresponding to the value at the black star). The grey dashed curve is based on the selected 0Ψ and 2Ψ damping parameters for different values of the 4Ψ parameter. The triangle and the square correspond to the models selected with the L-curve method for the $0\Psi + 2\Psi$ and $0\Psi + 2\Psi + 4\Psi$ inversions, respectively.
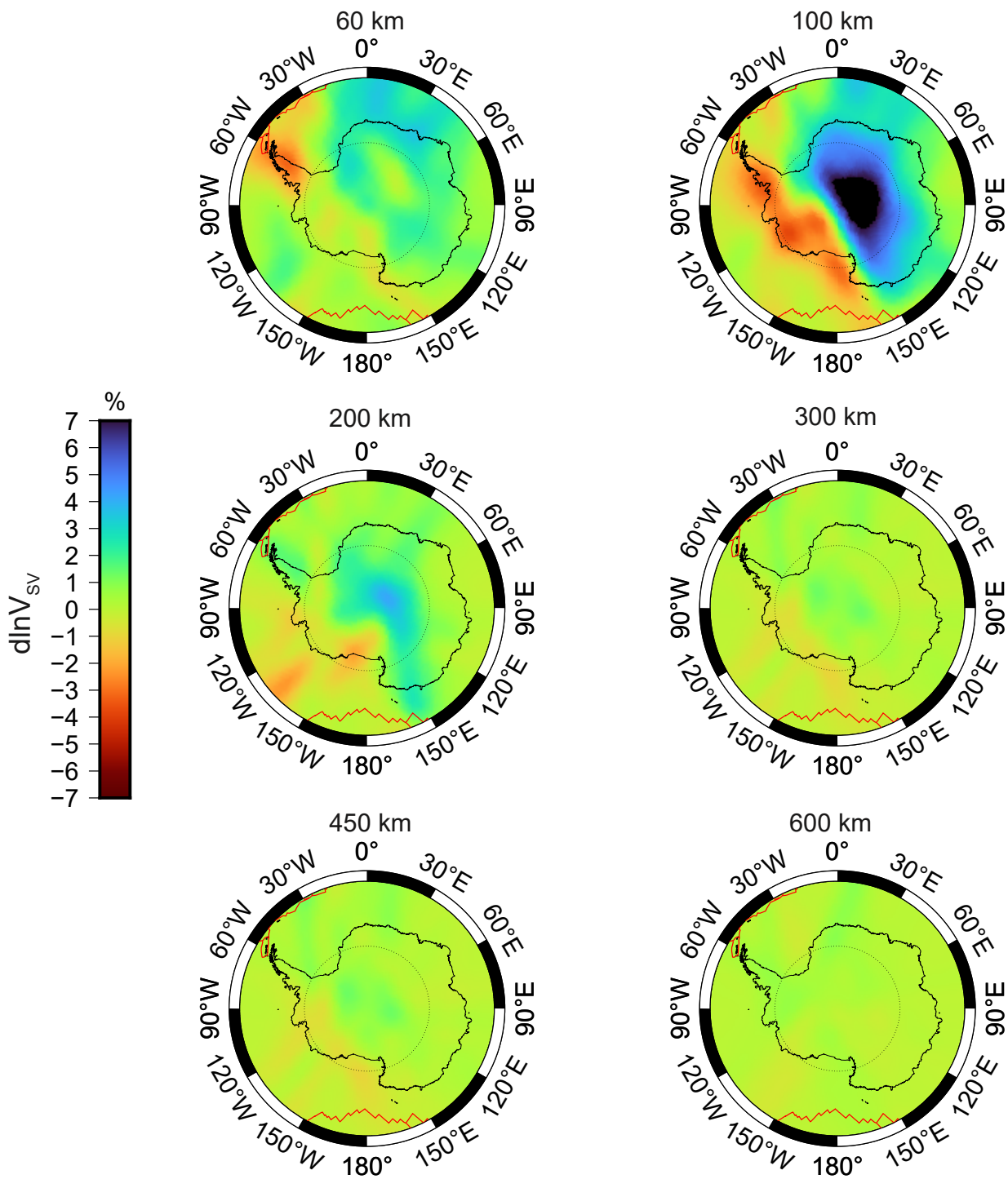
Figure 8   Isotropic part of our 3-D model at different depths. Perturbations are given with respect to PREM (Dziewonski and Anderson, 1981).
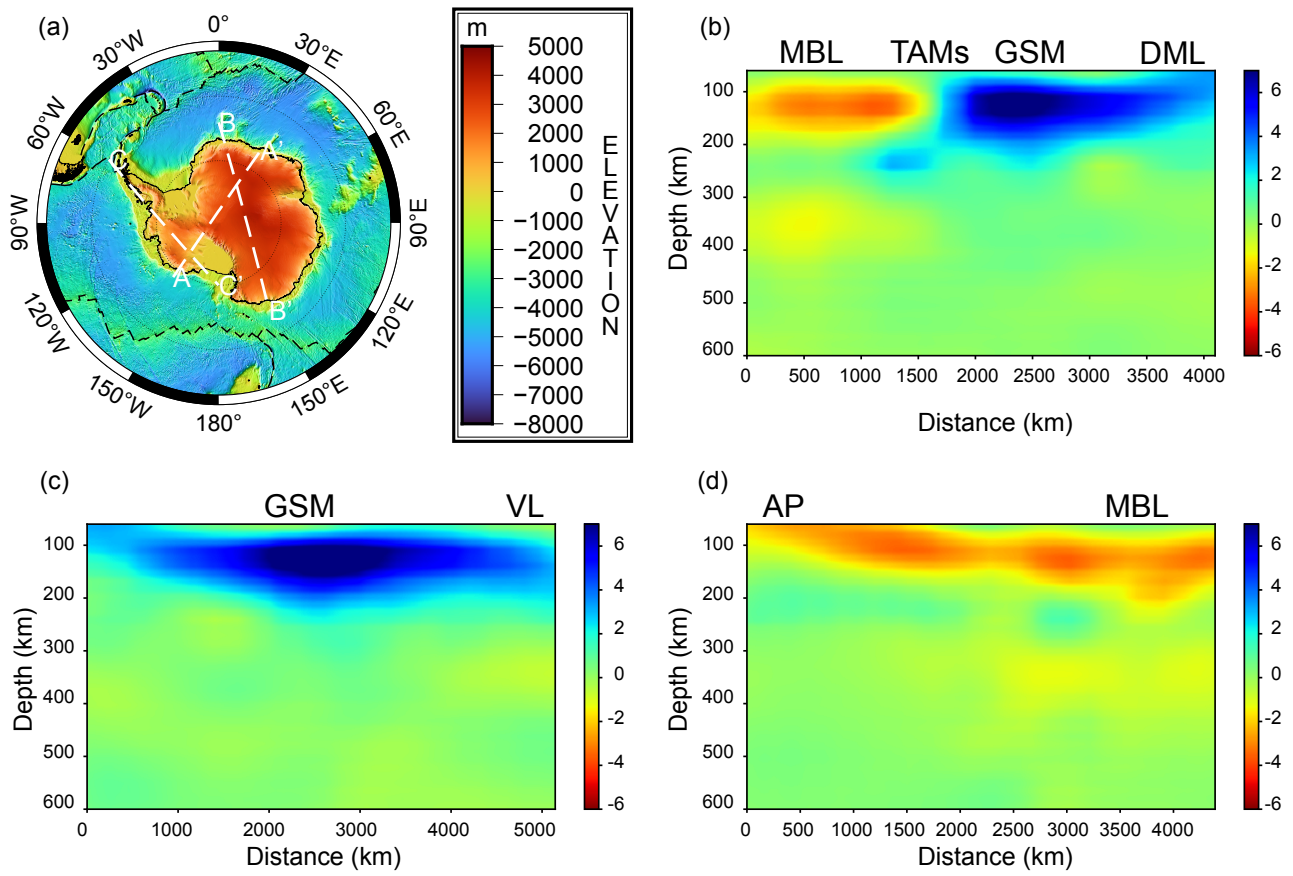
Figure 9 Cross sections of our 3-D isotropic model. V_S is shown along the transects shown by dashed lines in the topographic map of Antarctica (a): A-A'(b), which crosses EANT and WANT, B-B'(c), which samples EANT, and C-C'(c), which crosses WANT. Abbreviations: AP = Antarctica Peninsula; DML = Dronning Maud Land; GSM = Gamburtsev Subglacial Mountains; TAMs = Transantarctic Mountains; VL = Victoria Land.
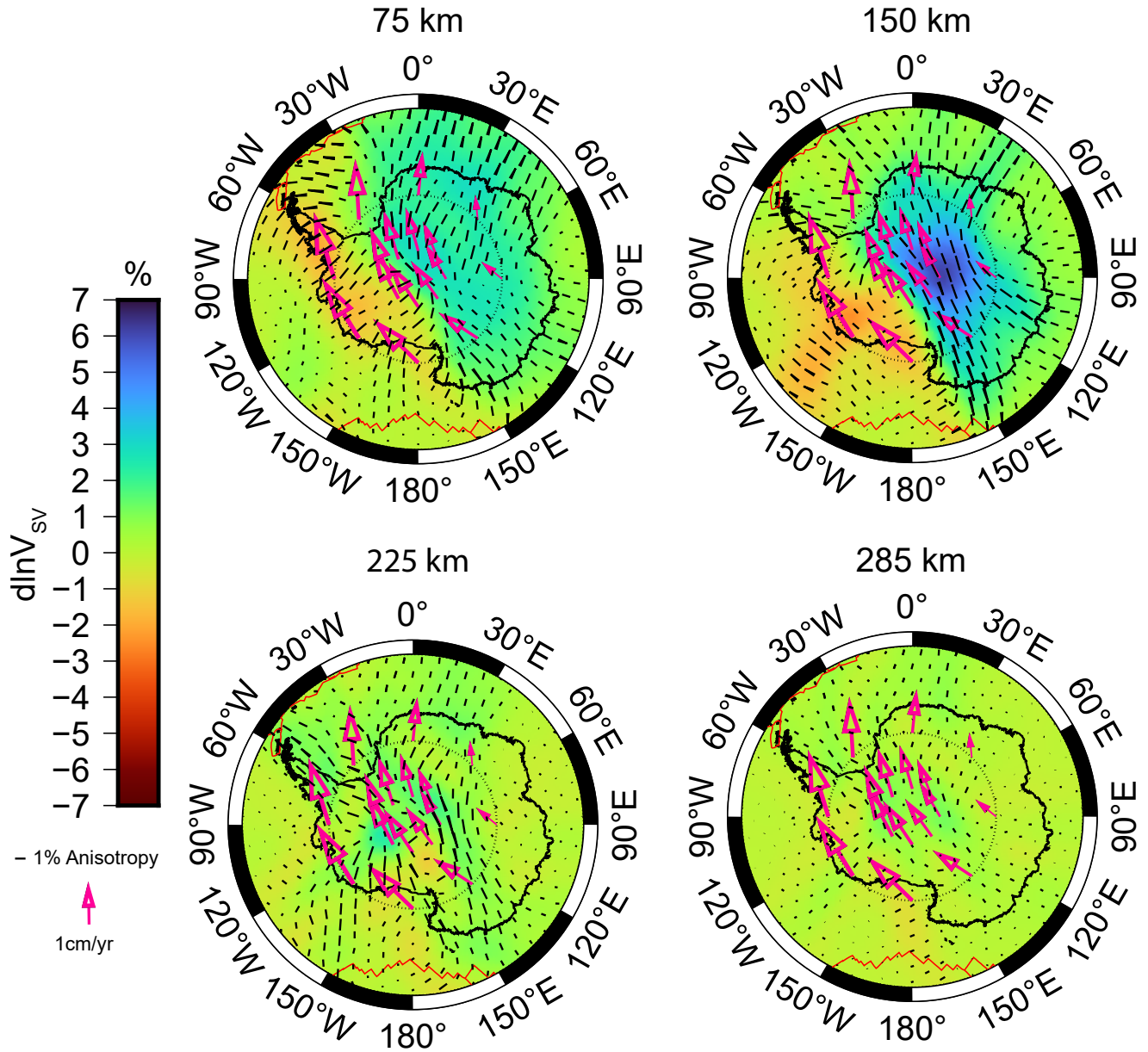
Figure 10 2Ψ anisotropy model at different depths superimposed onto the isotropic part of the model. The black bars represent the fast direction for V_{SV} propagation and the length of the black bars is proportional to the strength of the anisotropy. The magenta arrows represent the APM direction based on NUVEL-1A with no-net rotation reference frames (Gripp and Gordon, 2002).
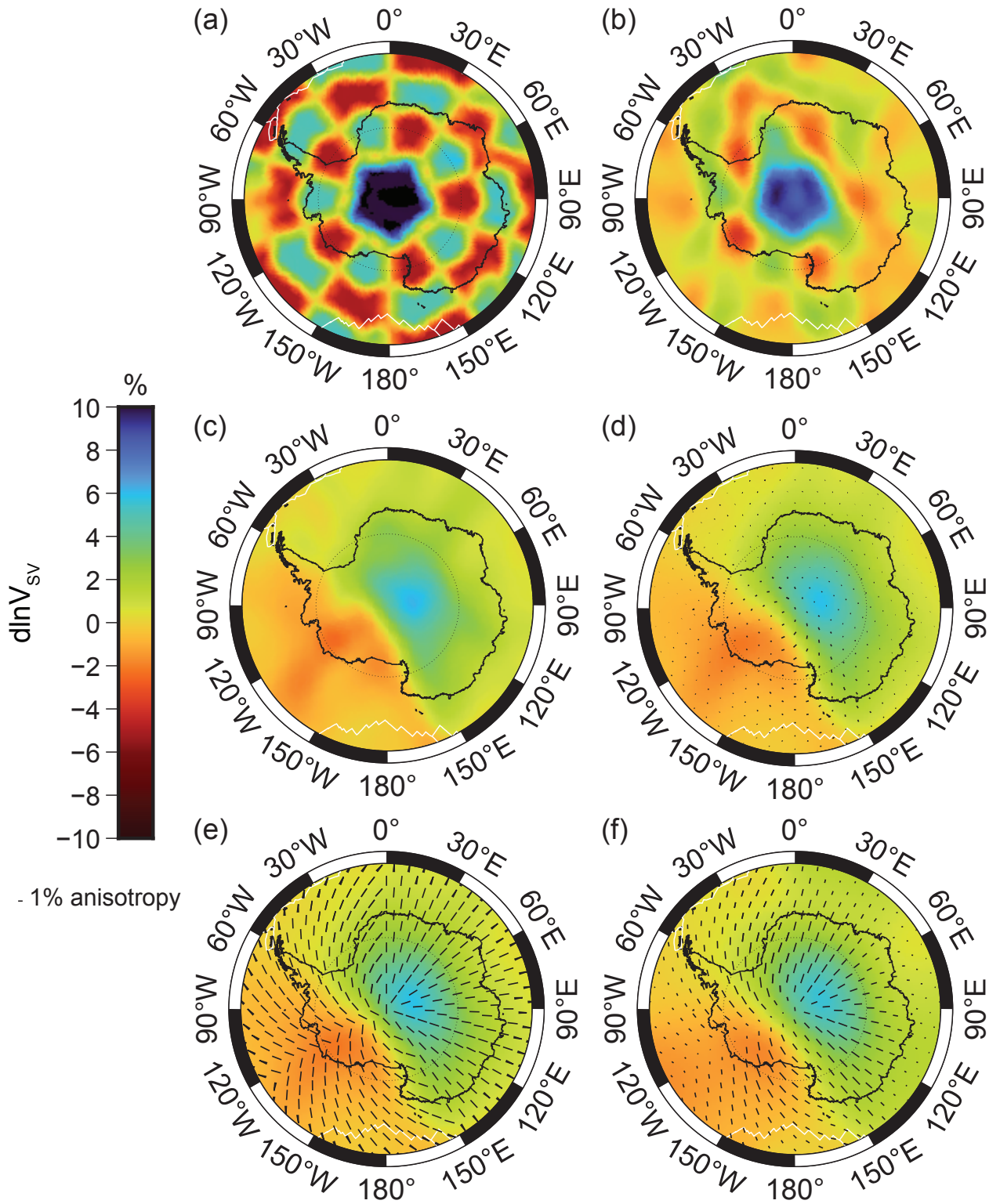
Figure 11   Synthetic tests at 150 km depth with the input models on the left and the corresponding output models on the right. (top): Isotropic checkerboard test; (middle): 2Ψ anisotropic inversion of an isotropic input model; (bottom): 2Ψ anisotropic resolution test. The length of the black bars represents the amplitudes of the anisotropy.
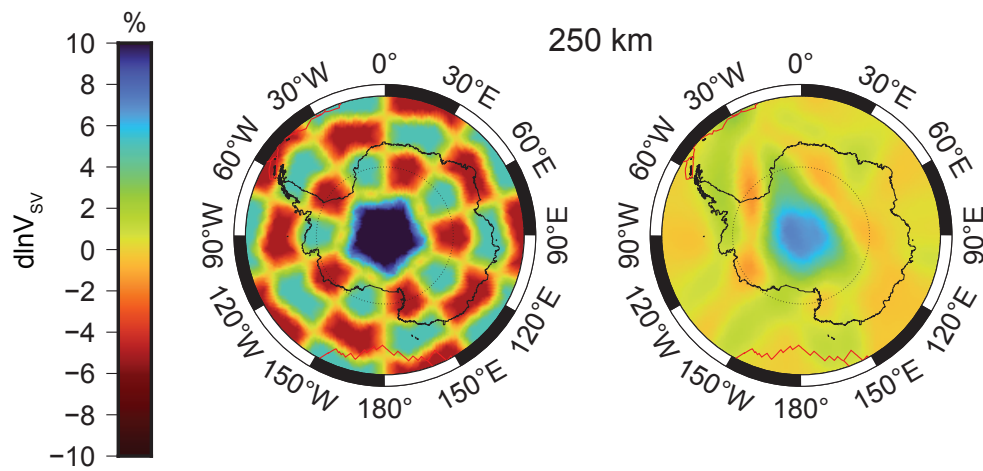
Figure 12 Synthetic tests at 250 km depth with isotropic checkerboard input model on the left and the corresponding output models on the right.
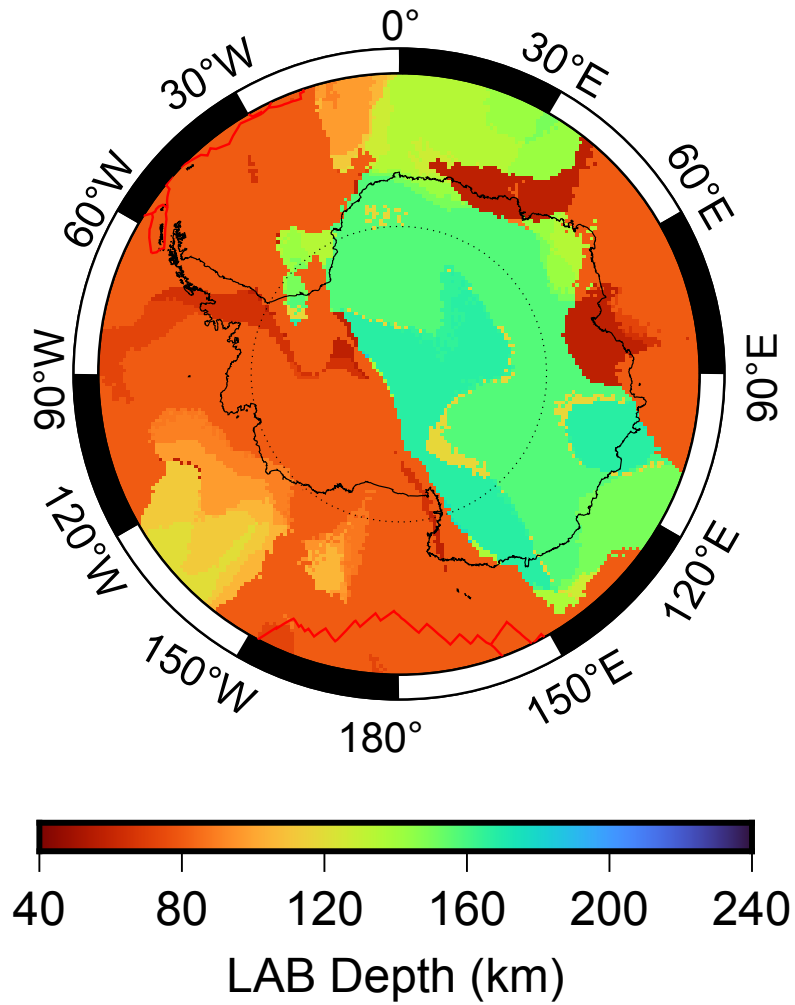
Figure 13 Map of the estimated LAB depth based on the middle of the interval over which V_{SV} decreases in the isotropic part of the model.
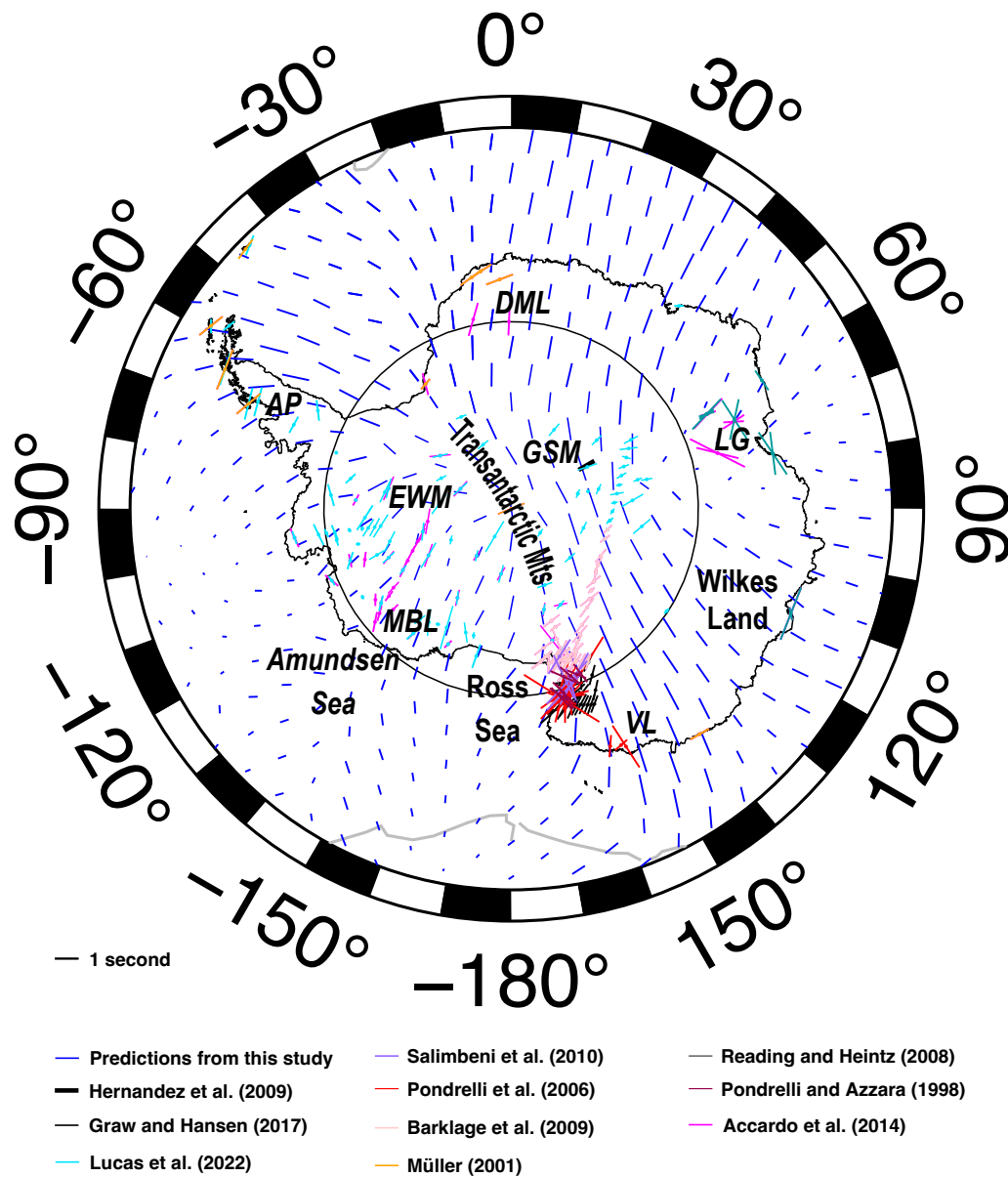
Figure 14 Predicted (blue) and observed shear-wave splitting for Antarctica. The thick black bar represents the overall splitting directions and study area from Hernandez et al. (2009). Others studies are from Pondrelli and Azzara (1998), Müller (2001), Pondrelli et al. (2006), Reading and Heintz (2008), Barklage et al. (2009), Accardo et al. (2014), Graw and Hansen (2017), and Lucas et al. (2022). The length of the bars is proportional to the splitting delay times. The plate boundaries are shown in grey. DML = Dronning Maud Land; EWM = Ellsworth-Whitmore Mountains; GSM = Gamburtsev Subglacial Mountains; LG = Lambert Graben; MBL = Marie Byrd Land; AP = Antarctica Peninsula; VL = Victoria Land.

Supplementary Information for "Azimuthal Anisotropy From Multimode Waveform Modeling Reveals Layering Within the Antarctica Craton" by Beghein, C. and Xu, H.

Table S1.: List of seismic stations employed in our study.

Network	Station	Latitude	Longitude
1D	S001	-84.5	-154.10
AI	BELA	-77.875	-34.6269
AI	DSPA	-53.953602	-68.266
AI	ESPZ	-63.398102	-56.996399
AI	JUBA	-62.237301	-58.662701
AI	ORCD	-60.738098	-44.736099
AI	SMAI	-68.130203	-67.105904
AU	MAW	-67.603996	62.870998
AU	MCQ	-54.4983	158.9403
AW	VNA3	-71.242	-9.666
C	GO07	-43.1142	-73.6644
C	GO08	-48.4648	-72.5566
C	GO09	-51.270699	-72.338097
C	GO10	-53.154598	-71.04979
C1	AY01	-44.42092	-72.64803
C1	AY03	-47.253042	-72.590769
C1	LL05	-41.405341	-73.47445
C1	MG01	-54.9322	-67.63
C1	MG02	-52.7808	-69.2242
C1	MG03	-53.84798	-70.46275
C1	MG04	-52.8572	-71.57
C1	MG05	-51.6784	-72.5032
G	CCD	-75.1065	123.305
G	COYC	-45.57299	-72.08139
G	CRZF	-46.43096	51.855308
G	DRV	-66.664908	140.002069
G	PAF	-49.351	70.210708
GE	SNAA	-71.6707	-2.8379
GT	PLCA	-40.73277	-70.55083
GT	VNDA	77.517275	161.852758
II	EFI	-51.6753	-58.0637
II	HOPE	-54.2836	-36.4879
II	TAU	-42.9099	147.3204
IU	CASY	-66.2792	110.5354
IU	PMSA	-64.7744	-64.0489

IU	QSPA	-89.9289	144.4382
IU	SBA	-77.8492	166.7572
IU	SNZO	-41.3087	174.7043
NZ	BFZ	-40.679647	176.246245
NZ	KHZ	-42.41598	173.53897
NZ	ODZ	-45.043982	170.644622
NZ	QRZ	-40.825522	172.529148
NZ	RPZ	-43.714608	171.053865
PS	SYO	-69.006699	39.584999
XD	PMC01	-77.849998	166.682007
XD	PMC02	-77.0	166.684998
XD	PSP02	-89.998001	81.777
XD	PSP03	-89.929001	144.360992
XH	DR16	-80.869499	178.430405
XH	RS08	-79.3899	-163.539398
XH	RS09	-79.424599	-159.848007
XH	RS11	-79.150398	-151.525894
XH	RS12	-79.017899	-147.632095
XH	RS13	-78.751503	-144.012299
XH	RS14	-78.474403	-140.457199
XH	RS15	-80.496597	-169.978806
XH	RS17	-81.401604	-162.973801
XH	RS18	-81.593697	177.334793
XJ	TRANB	-46.635441	-72.839523
Y3	FREW	-43.453701	171.904007
Y3	PDR01	-46.302399	-71.860802
YE	OBHI	-77.8504	-166.6843
YE	SPOLE	-89.93	144.44
YE	WERK	-77.8.73	166
YJ	CHC01	-46.541401	-71.7351
YJ	COC01	-47.2560	-72.592003
YJ	IMG01	-44.401699	-73.0914
YT	AGO1	-83.8615	129.6152
YT	AGO3	-82.7541	28.581
YT	ALYS	-84.3548	-23.7347
YT	BEAR	-74.5476	-111.8511
YT	BENN	-84.5731	-117.3923
YT	BYRD	-80.017	-119.4738
YT	CLRK	-77.3231	-141.8485
YT	DEVL	-81.4755	161.973
YT	DNTW	-76.4512	-107.7769
YT	DUFK	-82.8619	-53.2006

YT	FALL	-85.3066	-143.6284
YT	FISH	-78.9276	162.5652
YT	GM05	-81.1841	51.1587
YT	HOWD	-77.5286	-86.7694
YT	HOWE	-87.4158	-149.4267
YT	KOLR	-76.1544	-120.727
YT	LONW	-81.3466	152.735
YT	MA01	-76.9397	-97.5596
YT	MA02	-77.4394	-97.5595
YT	MA03	-77.9401	-97.5585
YT	MA04	-78.4221	-97.5879
YT	MA06	-79.4397	-97.5587
YT	MA07	-78.2496	-93.4991
YT	MA08	-77.4014	-103.0022
YT	MA09	-79.8993	-104.9977
YT	MA10	-78.5999	-109.0003
YT	MECK	-75.2808	-72.185
YT	MILR	-83.3063	156.2517
YT	MPAT	-78.0297	-155.0221
YT	N140	-82.0104	96.7558
YT	P061	-84.4997	77.2243
YT	PECA	-85.6124	-68.5525
YT	RMBO	-83.8714	-66.3959
YT	SILY	-77.1332	-125.966
YT	SIPL	-81.6405	-148.9553
YT	ST01	-83.228	-98.7418
YT	ST02	-82.069	-109.1247
YT	ST03	-81.4065	-113.1508
YT	ST04	-80.7152	-116.5792
YT	ST06	-79.3317	-121.8201
YT	ST07	-78.6388	-123.7953
YT	ST08	-77.9476	-125.5313
YT	ST09	-76.5309	-128.4734
YT	ST10	-75.8143	-129.7489
YT	ST12	-76.897	-123.816
YT	ST13	-77.5609	-130.5139
YT	ST14	-77.8378	-134.0802
YT	STEW	-84.1863	-86.2349
YT	SURP	-84.7199	-171.2017
YT	SWEI	-86.9858	129.3615
YT	THUR	-72.5301	-97.5606
YT	UNGL	-79.7746	-82.524

YT	UPTW	-77.5781	-109.0374
YT	WAIS	-79.4181	-111.7779
YT	WAWA	-81.5784	-28.4207
YT	WHIT	-82.6823	-104.3867
YT	WILS	-80.0396	-80.5587
YT	WNDY	-82.3695	-119.4135
ZJ	BEBP	-73.032547	156.869019
ZJ	DUBY	-74.985321	158.077316
ZJ	FOOT	-73.093414	157.853439
ZJ	GRAW	-74.004158	154.988647
ZJ	KNYN	-76.23735	153.326996
ZJ	MICH	-73.817101	164.099762
ZJ	RAPH	-73.59729	162.288467
ZJ	RKST	-74.201065	159.001755
ZJ	SAMH	-75.203033	153.99675
ZJ	SHRD	-73.398941	160.49884
ZJ	SPLN	-73.466217	161.471222
ZM	AGO1	-83.859596	129.612106
ZM	AGO3	-82.753998	28.583401
ZM	ALYS	-84.354897	-23.7342
ZM	GM01	-83.985802	104.729103
ZM	GM02	-79.425102	97.581497
ZM	GM03	-80.216904	85.943901
ZM	GM04	-82.999702	61.1124
ZM	GM05	-81.184097	51.158798
ZM	GM06	-79.332802	44.3148
ZM	GM07	-77.313599	39.613201
ZM	N100	-81.651703	122.590103
ZM	N124	-82.074501	107.640602
ZM	N132	-82.075104	101.9534
ZM	N140	-82.008598	96.769203
ZM	N148	-81.862503	91.507599
ZM	N156	-81.6726	86.504501
ZM	N165	-81.408401	81.760399
ZM	N173	-81.112198	77.473602
ZM	N182	-80.736298	73.189796
ZM	N190	-80.327499	69.431
ZM	N198	-79.859703	65.960701
ZM	N206	-79.394699	62.855598
ZM	N215	-78.904503	59.994301
ZM	P061	-84.499603	77.223801
ZM	P071	-83.6465	77.334702

ZM	P080	-82.805397	77.363998
ZM	P090	-81.936096	77.314201
ZM	P116	-79.566902	77.045097
ZM	P124	-78.871803	77.656998
ZM	SWEI	-86.985901	129.360703
ZT	WZ19	- 43.1129	170.580597

References

Albuquerque Seismological Laboratory (ASL)/USGS. (1993). Global Telemetered Seismograph Network (USAF/USGS) [Data set]. International Federation of Digital Seismograph Networks. https://doi.org/10.7914/SN/GT

Albuquerque Seismological Laboratory/USGS. (2014). Global Seismograph Network (GSN - IRIS/USGS) [Data set]. International Federation of Digital Seismograph Networks. https://doi.org/10.7914/SN/IU

Alfred Wegener Institute For Polar And Marine Research (AWI). (1993). AW – AWI Network Antarctica [Data set]. Deutsches GeoForschungsZentrum GFZ. https://doi.org/10.14470/NJ617293

Brisbourne, A., Stuart, G., and O'Donnell, J.P. (2016). UKANET: UK Antarctic Network. International Federation of Digital Seismograph Networks. https://doi.org/10.7914/SN/1D_2016

Chilean National Seismic Network. https://www.fdsn.org/networks/detail/C/

GEOFON Data Centre. (1993). GEOFON Seismic Network [Data set]. Deutsches GeoForschungsZentrum GFZ. https://doi.org/10.14470/TR560404

GNS Science. (2021). GeoNet Aotearoa New Zealand Seismic Digital Waveform Dataset [Data set]. GNS Science. https://doi.org/10.21420/G19Y-9D40

Geoscience Australia. (2021). Australian National Seismograph Network Data Collection (Version 2.0, September 2018). Commonwealth of Australia (Geoscience Australia). https://doi.org/10.26186/144675

Hansen, S.E., A.M. Reusch, T. Parker, D.K. Bloomquist, P. Carpenter, J.H. Graw, and G.R. Brenn (2015), The Transantarctic Mountains Northern Network (TAMNNET): Deployment and Performance of a Seismic Array in Antarctica, Seism. Res. Lett., 86, doi: https://doi.org/10.1785/0220150117.

Institut de physique du globe de Paris (IPGP), & École et Observatoire des Sciences de la Terre de Strasbourg (EOST). (1982). GEOSCOPE, French Global Network of broad band seismic stations. Institut de physique du globe de Paris (IPGP), Université de Paris. https://doi.org/10.18715/GEOSCOPE.G

Istituto Nazionale di Oceanografia e di Geofisica Sperimentale. (1992). Antarctic Seismographic Argentinean Italian Network - ASAIN [Data set]. International Federation of Digital Seismograph Networks. https://doi.org/10.7914/SN/AI

Pacific21 (ERI/STA). https://www.fdsn.org/networks/detail/PS/

Parker, T. and Beaudoin, B.. (2007). Development of A Power and Communication for Remote Autonomous GPS and Seismic Stations in Antarctica [Data set]. International Federation of Digital Seismograph Networks. https://doi.org/10.7914/SN/XD_2007

Russo, R.. (2004). Studies of crust and upper mantle structure, mantle flow and geodynamics of the Chile Ridge subduction zone [Data set]. International Federation of Digital Seismograph Networks. https://doi.org/10.7914/SN/YJ_2004

Russo, R. (2007). Studies of crust and upper mantle structure, mantle flow and geodynamics of the Chile Ridge subduction zone [Data set]. International Federation of Digital Seismograph Networks. https://doi.org/10.7914/SN/Y3_2007

Scripps Institution of Oceanography. (1986). Global Seismograph Network - IRIS/IDA [Data set]. International Federation of Digital Seismograph Networks. https://doi.org/10.7914/SN/II

Seismic Experiment in the Aisen Region of Chile (SEARCH). https://www.fdsn.org/networks/detail/XJ_2004/

Universidad de Chile. (2012). Red Sismologica Nacional [Data set]. International Federation of Digital Seismograph Networks. https://doi.org/10.7914/SN/C1

Wiens, D., Nyblade, A., and Aster, R.. (2007). IPY POLENET-Antarctica: Investigating links between geodynamics and ice sheets [Data set]. International Federation of Digital Seismograph Networks. https://doi.org/10.7914/SN/YT_2007

Wiens, D., and Aster, A.,. (2007). A Broadband Seismic Experiment to Image the Lithosphere beneath the Gamburtsev Mountains, East Antarctica [Data set]. International Federation of Digital Seismograph Networks. https://doi.org/10.7914/SN/ZM_2007

Wiens, D., Aster, A., and Bromirski, P.. (2014). Collaborative Research: Collaborative Research: Dynamic Response of the Ross Ice Shelf to Ocean Waves and Structure and Dynamics of the Ross Sea from a Passive Seismic Deployment on the Ross Ice Shelf [Data set]. International Federation of Digital Seismograph Networks. https://doi.org/10.7914/SN/XH_2014